

# Full calibration of the tomographic redshift distribution from the HSC PDR3 Shape Catalog with DESI

J. Choppin de Janvry <sup>1,2</sup> S. Gontcho A Gontcho <sup>1,3</sup> U. Seljak<sup>2,4</sup>  
A. Baleato Lizancos <sup>1,2</sup> E. Chaussidon <sup>1</sup> W. d'Assignies <sup>5</sup>  
J. DeRose <sup>6</sup> S. Heydenreich <sup>7</sup> E. Paillas <sup>8,9</sup> D. Valcin <sup>4</sup>  
T. Zhang<sup>10</sup> J. Aguilar<sup>1</sup> S. Ahlen <sup>11</sup> D. Bianchi <sup>12,13</sup> D. Brooks<sup>14</sup>  
F. J. Castander <sup>15,16</sup> T. Claybaugh<sup>1</sup> A. Cuceu <sup>1</sup> A. de la  
Macorra <sup>17</sup> P. Doel<sup>14</sup> S. Ferraro <sup>1,4</sup> A. Font-Ribera <sup>5</sup>  
J. E. Forero-Romero <sup>18,19</sup> E. Gaztañaga <sup>15,16,20</sup> G. Gutierrez<sup>21</sup>  
H. K. Herrera-Alcantar <sup>22,23</sup> K. Honscheid <sup>24,25,26</sup> M. Ishak <sup>27</sup>  
R. Joyce <sup>28</sup> S. Juneau <sup>28</sup> R. Kehoe<sup>29</sup> D. Kirkby <sup>30</sup>  
T. Kisner <sup>1</sup> A. Kremin <sup>1</sup> O. Lahav<sup>14</sup> C. Lamman <sup>26</sup>  
M. Landriau <sup>1</sup> L. Le Guillou <sup>31</sup> M. Manera <sup>5,32</sup> A. Meisner <sup>28</sup>  
R. Miquel<sup>5,33</sup> S. Nadathur <sup>20</sup> N. Palanque-Delabrouille <sup>1,23</sup>  
W. J. Percival <sup>34,35,36</sup> C. Poppett<sup>1,4,37</sup> F. Prada <sup>38</sup>  
I. Pérez-Ràfols <sup>39</sup> G. Rossi<sup>40</sup> E. Sanchez <sup>41</sup> D. Schlegel<sup>1</sup>  
M. Schubnell<sup>42,43</sup> J. Silber <sup>1</sup> D. Sprayberry<sup>28</sup> G. Tarlé <sup>43</sup>  
B. A. Weaver<sup>28</sup> R. Zhou <sup>1</sup>

<sup>1</sup>Lawrence Berkeley National Laboratory, 1 Cyclotron Road, Berkeley, CA 94720, USA

<sup>2</sup>Department of Physics, University of California, Berkeley, 366 LeConte Hall MC 7300, Berkeley, CA 94720-7300, USA

<sup>3</sup>University of Virginia, Department of Astronomy, Charlottesville, VA 22904, USA

<sup>4</sup>University of California, Berkeley, 110 Sproul Hall #5800 Berkeley, CA 94720, USA

<sup>5</sup>Institut de Física d'Altes Energies (IFAE), The Barcelona Institute of Science and Technology, Edifici Cn, Campus UAB, 08193, Bellaterra (Barcelona), Spain

<sup>6</sup>Physics Department, Brookhaven National Laboratory, Upton, NY 11973, USA

<sup>7</sup>Department of Astronomy and Astrophysics, UCO/Lick Observatory, University of California, 1156 High Street, Santa Cruz, CA 95064, USA

<sup>8</sup>Instituto de Estudios Astrofísicos, Facultad de Ingeniería y Ciencias, Universidad Diego Portales, Av. Ejército Libertador 441, Santiago, Chile

<sup>9</sup>Steward Observatory, University of Arizona, 933 N. Cherry Avenue, Tucson, AZ 85721, USA

- <sup>10</sup>Department of Physics & Astronomy and Pittsburgh Particle Physics, Astrophysics, and Cosmology Center (PITT PACC), University of Pittsburgh, 3941 O’Hara Street, Pittsburgh, PA 15260, USA
- <sup>11</sup>Department of Physics, Boston University, 590 Commonwealth Avenue, Boston, MA 02215 USA
- <sup>12</sup>Dipartimento di Fisica “Aldo Pontremoli”, Università degli Studi di Milano, Via Celoria 16, I-20133 Milano, Italy
- <sup>13</sup>INAF-Osservatorio Astronomico di Brera, Via Brera 28, 20122 Milano, Italy
- <sup>14</sup>Department of Physics & Astronomy, University College London, Gower Street, London, WC1E 6BT, UK
- <sup>15</sup>Institut d’Estudis Espacials de Catalunya (IEEC), c/ Esteve Terradas 1, Edifici RDIT, Campus PMT-UPC, 08860 Castelldefels, Spain
- <sup>16</sup>Institute of Space Sciences, ICE-CSIC, Campus UAB, Carrer de Can Magrans s/n, 08913 Bellaterra, Barcelona, Spain
- <sup>17</sup>Instituto de Física, Universidad Nacional Autónoma de México, Circuito de la Investigación Científica, Ciudad Universitaria, Cd. de México C. P. 04510, México
- <sup>18</sup>Departamento de Física, Universidad de los Andes, Cra. 1 No. 18A-10, Edificio Ip, CP 111711, Bogotá, Colombia
- <sup>19</sup>Observatorio Astronómico, Universidad de los Andes, Cra. 1 No. 18A-10, Edificio H, CP 111711 Bogotá, Colombia
- <sup>20</sup>Institute of Cosmology and Gravitation, University of Portsmouth, Dennis Sciama Building, Portsmouth, PO1 3FX, UK
- <sup>21</sup>Fermi National Accelerator Laboratory, PO Box 500, Batavia, IL 60510, USA
- <sup>22</sup>Institut d’Astrophysique de Paris. 98 bis boulevard Arago. 75014 Paris, France
- <sup>23</sup>IRFU, CEA, Université Paris-Saclay, F-91191 Gif-sur-Yvette, France
- <sup>24</sup>Center for Cosmology and AstroParticle Physics, The Ohio State University, 191 West Woodruff Avenue, Columbus, OH 43210, USA
- <sup>25</sup>Department of Physics, The Ohio State University, 191 West Woodruff Avenue, Columbus, OH 43210, USA
- <sup>26</sup>The Ohio State University, Columbus, 43210 OH, USA
- <sup>27</sup>Department of Physics, The University of Texas at Dallas, 800 W. Campbell Rd., Richardson, TX 75080, USA
- <sup>28</sup>NSF NOIRLab, 950 N. Cherry Ave., Tucson, AZ 85719, USA
- <sup>29</sup>Department of Physics, Southern Methodist University, 3215 Daniel Avenue, Dallas, TX 75275, USA
- <sup>30</sup>Department of Physics and Astronomy, University of California, Irvine, 92697, USA
- <sup>31</sup>Sorbonne Université, CNRS/IN2P3, Laboratoire de Physique Nucléaire et de Hautes Energies (LPNHE), FR-75005 Paris, France
- <sup>32</sup>Departament de Física, Serra Húnter, Universitat Autònoma de Barcelona, 08193 Bellaterra (Barcelona), Spain
- <sup>33</sup>Institució Catalana de Recerca i Estudis Avançats, Passeig de Lluís Companys, 23, 08010 Barcelona, Spain
- <sup>34</sup>Department of Physics and Astronomy, University of Waterloo, 200 University Ave W, Waterloo, ON N2L 3G1, Canada

<sup>35</sup>Perimeter Institute for Theoretical Physics, 31 Caroline St. North, Waterloo, ON N2L 2Y5, Canada

<sup>36</sup>Waterloo Centre for Astrophysics, University of Waterloo, 200 University Ave W, Waterloo, ON N2L 3G1, Canada

<sup>37</sup>Space Sciences Laboratory, University of California, Berkeley, 7 Gauss Way, Berkeley, CA 94720, USA

<sup>38</sup>Instituto de Astrofísica de Andalucía (CSIC), Glorieta de la Astronomía, s/n, E-18008 Granada, Spain

<sup>39</sup>Departament de Física, EEBE, Universitat Politècnica de Catalunya, c/Eduard Maristany 10, 08930 Barcelona, Spain

<sup>40</sup>Department of Physics and Astronomy, Sejong University, 209 Neungdong-ro, Gwangjin-gu, Seoul 05006, Republic of Korea

<sup>41</sup>CIEMAT, Avenida Complutense 40, E-28040 Madrid, Spain

<sup>42</sup>Department of Physics, University of Michigan, 450 Church Street, Ann Arbor, MI 48109, USA

<sup>43</sup>University of Michigan, 500 S. State Street, Ann Arbor, MI 48109, USA

E-mail: [jean.choppin@jeanvrydev@gmail.com](mailto:jean.choppin@jeanvrydev@gmail.com), [satya@virginia.edu](mailto:satya@virginia.edu), [useljak@berkeley.edu](mailto:useljak@berkeley.edu)

**Abstract.** The calibration of tomographic redshift distributions is essential for cosmological analysis of weak lensing data. In this work, we calibrate all four tomographic bins of the Hyper Suprime Camera (HSC) weak lensing catalog with the Dark Energy Spectroscopic Instrument (DESI) Data Release 1 and 2 using the clustering redshifts technique. We include  $z > 1.2$  redshift sources such as emission line galaxies (ELG) and quasars (QSO) sources in our calibration, which were not available in the previous HSC calibration (Rau et al. 2022, [1]), allowing a complete calibration of all the redshift bins. We find the first tomographic bin exhibits a small shift towards low redshifts. The second bin is in good agreement with the photometric calibration, while third and fourth bin exhibit a shift towards higher redshifts. However, these shifts are considerably smaller than the shifts obtained in the HSC Year 3 cosmic shear analyses. We evaluate the impact of galaxy bias and magnification effects from all the samples on the measurements, finding them to be small, and we propose corrections to reduce them further. We model the redshift distributions with splines and compare our results to previous analyses as well as to other parameterizations found in literature. For the two high-redshift tomographic bins, we find the shifts to higher redshifts with respect to the measurements performed in Rau+2022 to be  $\Delta z_3 = -0.039^{+0.020}_{-0.021}$  and  $\Delta z_4 = -0.048^{+0.012}_{-0.012}$ .

---

## Contents

<b>1</b>	<b>Introduction</b>	<b>1</b>
<b>2</b>	<b>Data</b>	<b>4</b>
2.1	DESI Large Scale Structure Catalog	4
2.2	HSC-SSP PDR3 Shape Catalog	6
<b>3</b>	<b>Modeling</b>	<b>7</b>
3.1	Density contrast	9
3.2	Integrating over small-scales	9
3.3	Building the $n(z)$ model	10
3.4	Galaxy bias for the photometric sample	11
3.5	Magnification	13
<b>4</b>	<b>Computing the two-point angular functions</b>	<b>16</b>
<b>5</b>	<b>Parametrization methods</b>	<b>19</b>
5.1	Combining tracers	19
5.2	Suppressed Gaussian Processes	20
5.3	B-spline parametrization	20
<b>6</b>	<b>Results</b>	<b>22</b>
<b>7</b>	<b>Conclusion</b>	<b>26</b>
<b>A</b>	<b>Tomographic bin widths in the photometric galaxy bias approximation</b>	<b>34</b>

---

## 1 Introduction

With the current and upcoming generations of large-scale optical imaging surveys, such as the Hyper Suprime-Cam Subaru Strategic Program (HSC-SSP, [2]), the Dark Energy Survey (DES, [3]), the Kilo-Degree Survey (KiDS, [4]), the Nancy Grace Roman Space Telescope [5], Euclid [6] and the Vera C. Rubin Observatory’s Legacy Survey of Space and Time (LSST, [7]) probing hundreds of millions to billions of galaxies with accurate shape information, the strength of cosmological parameter inference from weak lensing analysis is becoming increasingly important. Some of the most precise single measurements of the lensing amplitude  $S_8 \equiv \sigma_8 \sqrt{\Omega_m/0.3}$  currently come from cosmic shear analyses [8–13], where one measures the correlation in the distortion of galaxy images due to weak gravitational lensing.

These optical surveys rely on characterization of their normalized sample redshift distributions projected along the line of sight  $n(z)$  when measuring two-point statistics of galaxy clustering and gravitational shear fields for cosmological parameter inference, most often performed through the two-point correlation functions [8] or the angular power spectrum [9]. Since optical surveys rely on broadband photometry covering optical and near-infrared wavelengths, narrow spectral galaxy features such as emission lines are difficult to identify due to the limited coverage per observed object and the broadband nature of the optical filters.

Therefore, imaging surveys employ photometric redshift (photo- $z$ ) algorithms to infer individual redshifts. Typically, photometric redshifts are used to split the galaxies into tomographic redshift bins, and the true redshift distribution along the line of sight needs to be estimated for each bin. One can reconstruct the overall redshift distribution  $n(z)$  from observed data for each tomographic bin. In the case of the fiducial HSC Year 3 analysis [1, 8, 9], four tomographic bins are used, spanning linear bins from  $z_p \sim 0.3$  to  $z_p \sim 1.5$ , where  $z_p$  here is a photometric redshift from a given photo- $z$  method. Henceforth, Bin 1 refers to  $0.3 \leq z_p < 0.6$ , Bin 2 to  $0.6 \leq z_p < 0.9$ , Bin 3 to  $0.9 \leq z_p < 1.2$  and Bin 4 to  $1.2 \leq z_p < 1.5$  respectively. Many different algorithms have been developed for photometric redshifts, ranging from inferring redshifts based on prior knowledge of galaxy spectral energy distributions (SEDs) ([14–17]) to mapping redshifts to photometry information with machine learning ([18–20]). Often, since the performance of the algorithms does not allow for perfect point estimates of the redshift, photo- $z$  methods will instead provide a probability density function (PDF) for each source, which allows for more information on how likely the point estimate is for a given photo- $z$  algorithm. If photometric redshifts were perfectly calibrated, the convolution of these PDFs would accurately describe the PDF  $n(z)$  for the tomographic bins. This is not possible in practice due to the performance limitations of photo- $z$  algorithms with limited spectroscopic training sets.

Thus, challenges arise when debiasing and calibrating the redshift distributions obtained by the chosen photo- $z$  algorithm(s), and as a result, weak lensing cosmological analyses can suffer from this systematic. Differences in tomographic redshift calibration can lead to significant cosmological parameter shifts, as demonstrated by Figure 1 of [1] or by the differences in calibrations on the KiDS-Legacy dataset [13, 21], compared to the analysis performed on KiDS-1000 [12]. Another approach taken by the HSC team was to parametrize photometric redshift uncertainty using a free shift parameter of the redshift first moment for the higher redshift tomographic bins lacking good redshift calibration. While this can encompass systematics, it in turn weakened the obtained cosmological information on  $S_8$  and  $\Omega_m$  [8, 9]. Moreover, this self-calibration approach requires that the parameterization of the error in the redshift distribution is accurate.

To mitigate the weaknesses of photo- $z$  algorithms and to debias the photo- $z$  distributions, a number of methods have been developed to calibrate the sample redshift distribution of each bin. A popular approach is to rely on the optical photometry information given by the survey and known spectroscopic redshifts from external datasets to infer redshift distributions from the galaxy population color-space, often using data reduction algorithms and machine learning methods. This technique is commonly executed with Self-Organizing Maps (SOM) [22–26], or through direct weighted calibration [27]. The limiting factor of this approach is often the source depth and color-space coverage of spectroscopic surveys, as spectroscopic redshift targets are more prone to failures and need longer integration times on faint targets with few easily discernible features for spectroscopy.

Another method is to use the clustering of galaxies: by leveraging angular cross-correlations between a spectroscopic sample in small redshift slices and the galaxies in each of the tomographic bins of the weak lensing survey dataset, the technique known as clustering redshifts allows to debias [1, 21, 28–39] the  $n(z)$  distributions. This is the method employed in this work. However, clustering redshifts is also subject to systematics, since the method benefits from information of small angular scales (typically  $0.1 - 5h^{-1}\text{Mpc}$ ) yielding higher signal to noise, though galaxy bias modeling at these scales remains difficult. In this work, common possible systematics that can affect and bias the clustering redshifts calibration of the pho-

tometric sample are investigated, such as the impacts of galaxy bias and magnification. This methodology is applied to the S19A Shape Catalog [40] from the Hyper Suprime-Cam Subaru Strategic Survey Public Data Release 3 [2] (S19A HSC-SSP PDR3) as our photometric catalog to calibrate. Hereafter, we refer to this dataset simply as HSC. The Dark Energy Spectroscopic Instrument Data Release 1 [41] and Data Release 2 [42] (DESI DR1, DR2) will serve as our spectroscopic calibration samples.

The Dark Energy Spectroscopic Instrument (DESI) is a Stage IV spectroscopic survey [43–45] carrying out a eight year program that started collecting data in 2021. DESI uses a focal plane hosting 5000 robotic positioners containing optical fibers [46] to obtain spectra, and therefore accurate spectroscopic redshifts [47], from galaxies. DESI plans to probe 17,000 deg<sup>2</sup> of the sky in its main phase of operations [48], covering spectroscopic redshift ranges up to  $z \sim 4.2$ . The DESI experiment studies six different types of tracers: the Milky Way Survey, observing stars in our local galaxy, the Bright Galaxy Survey (BGS,  $0.01 \lesssim z \lesssim 0.6$ ) [49], the Luminous Red Galaxies (LRG,  $0.3 \lesssim z \lesssim 1.2$ ) [50], the Emission Line Galaxies (ELG,  $0.7 \lesssim z \lesssim 1.6$ ) [51], the Quasi-Stellar Objects (QSO,  $0.7 \lesssim z \lesssim 2.1$ ) [52] and the Lyman- $\alpha$  forest ( $\text{Ly}\alpha$ ,  $z \gtrsim 2.1$ ). With its accurate redshift catalog, DESI has already allowed for significant breakthroughs on cosmological measurements [53, 54].

The Hyper Suprime-Cam Subaru Strategic Program<sup>1</sup>[55] is a Stage 3 optical imaging survey using the Hyper Suprime-Cam wide-field camera installed on the Subaru 8.2m telescope on the summit of Maunakea, Hawai’i, and covers three depth layers: the Wide field, the Deep field, and Ultra-Deep field. The S19A (from the the internal September 2019 data release) Shape Catalog [40] compiles galaxy shapes from  $i_{\text{band}}$  imaging data obtained from 2014 to 2019 in the Wide field of the HSC-SSP. It is crucial to obtain well calibrated redshift distributions of this dataset, as constraints from cosmic shear heavily depend on this larger area.

In the tomographic bin analysis performed by the HSC collaboration [1], there was no calibration from angular clustering of galaxies above  $z \gtrsim 1.2$  due to the redshift limitations of the LRG dataset used in that study, therefore not providing calibration information from clustering redshifts for most of Bin 3 and none for Bin 4. On the color-redshift calibration aspect, lack of high redshift spectroscopic sources and deep infrared photometry led to degeneracies that made for difficult calibration. In turn, this makes the mean value from the fiducial calibration of a given redshift bin uncertain, meaning that major shifts are possible on Bins 3 and 4. Indeed, analysis by [56] showed a single shift parameter was sufficient to capture  $n(z)$  uncertainty per bin in the HSC distributions. The cosmic shear analyses on the two-point correlation function [8] and on the angular power spectrum [9] of HSC used a conservative uniform prior  $\mathcal{U}([-1, 1])$  for the tomographic bins redshift shift parameters. Both analyses report hints of photo- $z$  miscalibration, with possible redshift expectation values being higher than initially obtained from the redshift bins only calibrated with photometry. Reported marginalized mode of shifts with asymmetric 34% confidence interval and maximum a posteriori (MAP) values of shifts obtained by both HSC cosmic shear analyses have returned<sup>2</sup>:  $\Delta z_3 = -0.075_{-0.059}^{+0.056}(-0.046)$  and  $\Delta z_4 = -0.157_{-0.111}^{+0.094}(-0.144)$  for the angular power spectrum [9] and  $\Delta z_3 = -0.115_{-0.058}^{+0.052}(-0.120)$  and  $\Delta z_4 = -0.192_{-0.088}^{+0.088}(-0.190)$  for the angular two point correlation functions [8] in Bin 3 and Bin 4. More recent works [57] used Cosmic Shear Ratios (CSR) in order to provide calibration for the photometric redshift bins, while [58] leverages galaxy clustering and weak lensing (GC-WL) to infer constraints

---

<sup>1</sup>[hsc-release.mtk.nao.ac.jp/doc/](https://hsc-release.mtk.nao.ac.jp/doc/)

<sup>2</sup>Note the following convention: a negative shift implies the found expectation value (from cosmic shear analysis) for a bin is higher than the available measurements.

on the source redshift bins. While the results found by that calibration are consistent with those obtained by the cosmic shear analyses, the error bars loosely constrain the redshift expectation: the obtained results were  $\Delta z_3 = -0.002^{+0.085}_{-0.217}$ ,  $\Delta z_4 = -0.292^{+0.229}_{-0.324}$  for the CSR study and  $\Delta z_3 = -0.112^{+0.046}_{-0.049}$ ,  $\Delta z_4 = -0.185^{+0.071}_{-0.081}$  for the GC-WL analysis. In this work, the focus will be on constraining these two shift parameters, comparing results to the HSC analyses as well as previous calibrations, and producing  $n(z)$  distributions for each of the bins.

The outline of this paper is as follows. Section 2 presents the datasets employed in this study: HSC’s Shape catalog and DESI DR1, DR2, as well as the quality cuts applied to both catalogs. Section 3 describes the modeling of the  $n(z)$  distributions with two-point correlation functions and discusses systematic effects, including galaxy bias from both samples and magnification effects. Section 4 describes our measurements of the angular correlation vectors. Section 5 presents a spline based approach to model the  $n(z)$  distributions and discusses other methods to regularize the clustering redshifts measurements. Finally, results are showcased in section 6.

## 2 Data

This section describes the datasets and catalogs used in this analysis. DR1 refers to DESI Data Release 1<sup>3</sup>[41], and DR2 refers to DESI Data Release 2. Data for DR1 was obtained with main survey observations spanning May 2021 to June 2022, while data for DR2 spans May 2021 to April 2024. To this, data releases also include survey validation observations from December 2020 to May 2021. Compliance with DESI internal policies required the use of DESI DR2 to be limited to the calibration of the two highest HSC tomographic bins:  $0.9 < z_p \leq 1.2$  and  $1.2 < z_p \leq 1.5$ . We use the public DESI DR1 dataset for the remaining tomographic bins:  $0.3 < z_p \leq 0.6$  and  $0.6 < z_p \leq 0.9$ , where  $z_p$  is the photometric redshift derived from HSC presented in section 2.2. For measurements on tomographic bins different from the fiducial HSC [1, 8, 9] ones (for example, in section 3.4), DR1 is used for any tomographic bin such that  $z_p \lesssim 0.9$ , and DR2 elsewhere ( $z_p > 0.9$ ), where  $z_p$  is the center of the tomographic bin in photometric redshift. The DESI dataset is further described hereafter, in section 2.1. The photometric sample we calibrate is the S19A HSC-SSP PDR3 Shape Catalog (HSC) [40], described in 2.2. The three catalogs’ footprints are displayed in Figure 1.

### 2.1 DESI Large Scale Structure Catalog

For both DESI DR1 and DR2, calibrations are performed with the Large Scale Structure (LSS) catalogs of the DESI survey [59]. The LSS catalogs provide weighted clustering and random catalogs tailored to the specifics of the DESI survey for each of the target classes used. The LSS catalogs take into account imaging systematics, selection and footprint effects, possible redshift failures, tiling overlap, as well as other effects – the full description of which can be found in the DESI data model<sup>4</sup> and in in refs [59, 60].

This work uses multiple target classes: the BGS [49], the LRGs [50], the ELGs [51] and the QSOs [52] as described above. The target classes’ redshift ranges used in this study are described in Table 1, per data release, and the redshift density distribution for both data releases over the HSC footprint is showcased in Figure 2. DESI uses priority ranking to perform fiber assignment on targets [46]. For the BGS sample, this work uses the BGS\_ANY

<sup>3</sup>[data.desi.lbl.gov/doc/releases/dr1/](https://data.desi.lbl.gov/doc/releases/dr1/)

<sup>4</sup>[desidatamodel.readthedocs.io/LSSCats](https://desidatamodel.readthedocs.io/LSSCats)

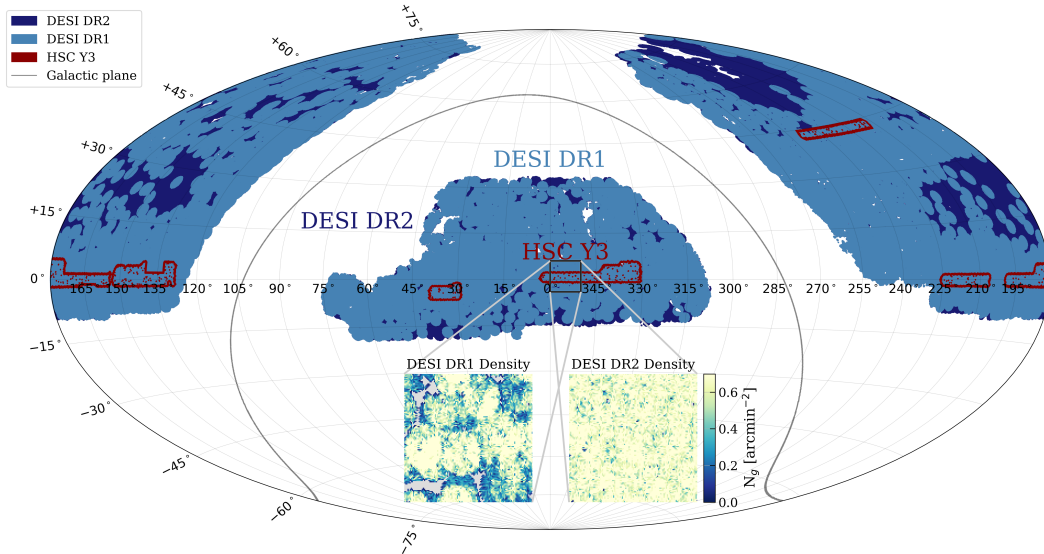


**Figure 1:** Sky coverage of DESI DR2 [42] (dark blue), DR1 [41] (light blue, overlapping DR2) and HSC Year 3 Shape Catalog [40] (red outline), with the galactic plane (gray line). An area centered around RA  $\sim 355^\circ$ , DEC  $\sim 0^\circ$  is highlighted with density maps to compare the coverage of DESI DR1 and DR2 of the same area covering a chunk of the footprint of HSC Y3’s WDS field. The HSC data lands in areas of high overall completeness for DESI, as these areas were targeted in priority. DESI DR2 improves over DR1 with better overall completeness, especially for the ELGs and in the northern HECTOMAP field (roughly RA  $\sim 40^\circ$ , DEC  $\sim 240^\circ$ ).

sample, which includes both the BGS\_BRIGHT and BGS\_FAINT samples, and hereafter referred to as BGS. More details can be found in the BGS selection description, under section 3 of [49]. For the ELG sample, we decide to not use DR1 ELGs in this work, as their very low completeness interferes with the auto-correlation measurements and provides only little information for the two first tomographic bins due to low redshift overlap. In DR2, as shown by Figure 1, the local density is much higher and we can now measure auto-correlation of ELGs in this context. For the ELG sample, this analysis uses the LOW-Priority (LOP) sample [51] preferentially selects high redshift ELGs at  $1.1 \lesssim z \lesssim 1.6$ . In DR2, in addition to LOP, we use the Very LOW priority (VLO) sample for ELGs, which focuses on targets in  $0.6 \lesssim z \lesssim 1.1$ . Indeed, the inclusion of VLO to the LSS catalogs is a new feature of DR2 compared to DR1, as displayed in figure 2.

**Table 1:** Redshift ranges as inclusive bin edges used for each data release per tracer.

Tracer	DR1	DR2
BGS	0 – 0.5	0 – 0.6
LRG	0.4 – 1.1	0.3 – 1.2
ELG (LOP+VLO)	-	0.7 – 1.6
QSO	0.8 – 2.8	0.7 – 2.8

Note that for DR2, some sources are expected outside of the bounds described in Table 1 and shown in Figure 2. Their lower number densities and negligible overlap with the two

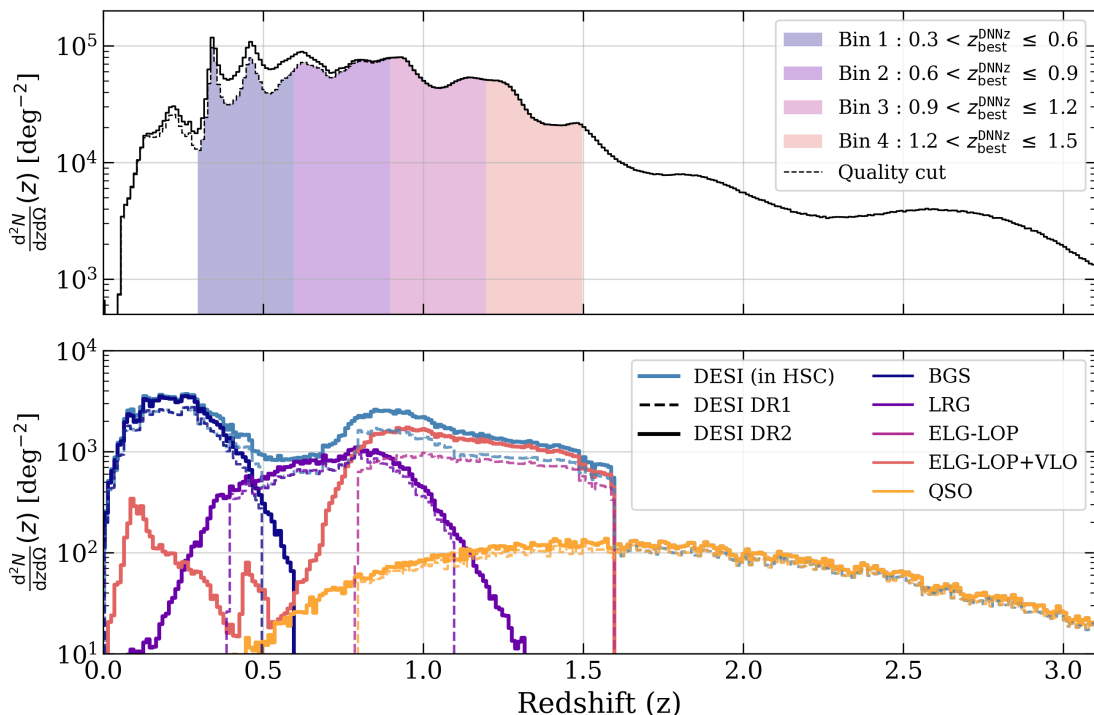


**Figure 2:** *Upper panel:*  $N(z)$  angular density per redshift from the HSC catalog, using photometric redshifts from the DNNz algorithm [61]. The effect of the calibration cut on HSC is displayed, removing problematic sources up to  $z_{\text{best}}^{\text{DNNz}} \leq 0.9$  (dotted histogram), as well as HSC’s four tomographic bin selections (shaded colors, including the calibration cut). *Lower panel:*  $N(z)$  angular density per redshift of the DESI Large Scale Structure clustering catalogs [59], showcasing the combined tracers distribution (light blue) in the HSC footprint and individual tracers (BGS, ELG, LRG and QSOs). DR1 is represented in dotted lines and DR2 is represented in full lines. In this figure, ELGs are distinguished between ELG-LOP (DR1 analysis) and ELG-LOP+VLO (DR2 analysis). Since most of the HSC footprint is already included in DR1, adding DR2 does not provide an improvement as big as one could expect, though there still are density differences as showcased in Figure 1. Per tomographic bin, the effective number density counts of photometric sources are 3.77, 5.07, 4.00 and 2.12 arcmin $^{-2}$  [62] after applying the calibration cut.

highest redshift tomographic bins of HSC motivates our choice for redshift cuts. For example, information from low redshift ELGs ( $\lesssim 0.7$ ) is not included.

## 2.2 HSC-SSP PDR3 Shape Catalog

The weak lensing catalog calibrated in this study is the S19A galaxy shape catalog [40] provided by the Public Data Release 3 (PDR3) [2] of the Hyper Suprime-Cam Subaru Strategic Program. This catalog builds upon  $i_{\text{band}}$  imaging data obtained from 2014 to 2019 in the Wide fields of the HSC survey, at a mean  $i_{\text{band}}$  seeing of  $0.59''$  [40]. A conservative  $i_{\text{band}} < 24.5$  magnitude cut is applied to the dataset. The catalog itself is split into 6 fields named HECTOMAP, XMM, VVDS, GAMA09H, GAMA15H and WIDE12H.

As a preliminary step, a *calibration cut* is applied to the first two tomographic bins of the HSC shape catalog. It removes  $\sim 31\%$  of sources in the first bin, and  $\sim 8\%$  of

sources in the second bin. The cut, shown in equation 2.1, is not applied on the third and fourth bin. This selection is performed in order to remove possible outliers in the individual probability density functions from the photo- $z$  algorithm reporting multi-modal distributions with a second, smaller peak around  $z \sim 3$ . The cut depends on the 95% confidence interval boundaries of the DNNz [61] and Mizuki [17] photometric redshift algorithms, such that:

$$(z_{95, \max}^{\text{DNNz}} - z_{95, \min}^{\text{DNNz}}) < 2.7 \ \& \ (z_{95, \max}^{\text{Mizuki}} - z_{95, \min}^{\text{Mizuki}}) < 2.7 \quad (2.1)$$

Moreover, for the rest of this analysis, when using redshifts outside of the HSC tomographic bins, the calibration cut is applied to all sources with redshifts between  $z \sim 0$  and  $z \sim 0.3$ . This removes about  $\sim 16\%$  of the sources within that redshift range. Redshifts outside the fiducial tomographic bins are used to evaluate galaxy bias evolution for HSC, in section 3.4. The fiducial redshift value kept to determine if a redshift is included in a bin or not is  $z_{\text{best}}^{\text{DNNz}}$ . The  $_{\text{best}}$  subscript notes the redshift point estimate that minimizes the risk function,  $R(z_p) = \int P(z)L(\frac{z_p - z}{1+z})dz$ , based on the individual probability density function  $P(z)$  obtained through DNNz, and with  $L(x)$  a loss function. More details can be found in the following works [61, 63].

### 3 Modeling

This section describes the modeling choices and assumptions used to model the sample redshift distributions in the tomographic bins. We first present the estimator used to infer the photometric sample redshift distribution  $n_p(z)$  for each bin, then discuss further corrections to potential systematic effects affecting this measurement, such as correcting for magnification effects and photometric sample galaxy bias. One can express the observed projected galaxy density contrast at position  $\hat{\theta}$  as the contribution of clustering and magnification [35, 64]:

$$\delta_x^{\text{obs}}(\hat{\theta}) = \delta_x^{\text{g}}(\hat{\theta}) + \delta_x^{\mu}(\hat{\theta}) \quad (3.1)$$

where  $\delta_x^{\text{g}}$  is the line of sight projection of the three dimensional galaxy contrast for galaxy sample  $x$  and  $\delta_x^{\mu}(\hat{\theta})$  is the magnification term. Specifically:

$$\delta_x^{\text{g}}(\hat{\theta}) = \int n_x(z)\delta_x^{\text{g}}(z, \hat{\theta})dz \quad (3.2)$$

where  $\delta_x^{\text{g}}(z, \hat{\theta})$  is the 3D galaxy contrast and  $n_x(z)$  is the distribution of galaxies in the considered sample  $x$ . Under the assumption that the universe is isotropic,  $\theta$  will now be treated as a scalar variable. When it comes to measuring the angular two-point correlations, one can write [35]:

$$\omega_{x,y}(\theta) = \omega_{x,y}^{\text{g} \times \text{g}}(\theta) + \omega_{x,y}^{\mu \times \text{g}}(\theta) + \omega_{x,y}^{\text{g} \times \mu}(\theta) \quad (3.3)$$

where  $\omega_{x,y}^{\text{A} \times \text{B}} = \langle \delta_x^{\text{A}} \delta_y^{\text{B}} \rangle(\theta)$  with A, B the respective contributions for sample  $x$  and  $y$ . The dominant contribution to the angular two-point correlation is the galaxy contrast ( $\text{g} \times \text{g}$ ). Corrections related to magnification effects ( $\mu \times \text{g}$ ,  $\text{g} \times \mu$ ) are presented in section 3.5. Higher order terms, such as  $\mu \times \mu$ , are not considered due to being subdominant with respect to any contribution including the galaxy density contribution  $\text{g}$ . Redshift Space Distortions (RSD) are also neglected in our analysis: such contributions were shown to be negligible for wide projections and small scales used here [65].

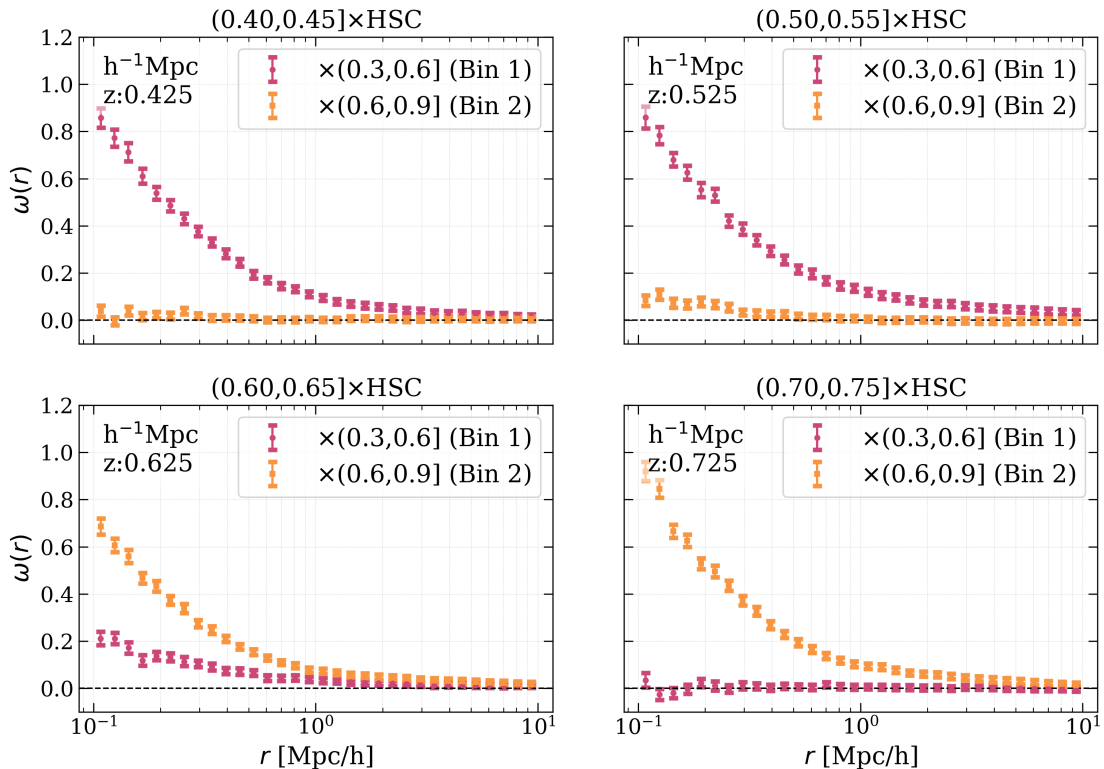


**Figure 3:** Example cross-correlation measurements for small spectroscopic slices with HSC bins. Here, the spectroscopic sources are DR1 LRGs, cross-correlated with the first two HSC tomographic bins. Comoving distance is computed at the redshift highlighted in the top left corner of each plot. As the redshift increases, one can see the weaker integrated signal for cross correlations with the first tomographic bin (purple), since the  $n(z)$  decreases when far away from the photo- $z$  boundaries, and the stronger signal for the second tomographic bin as the redshifts reaches  $z \sim 0.6 - 0.9$  (orange).

In most clustering redshift analyses, at least one of the samples (say,  $n_x$ ) is considered in sufficiently narrow redshift bins such that the distribution of each of the bins can be approximated as an indicator function of the redshift interval. Our fiducial bin size for the spectroscopic sample is  $\Delta z_s = 0.05$ , which is sufficient to capture the shape of distributions as large as the HSC tomographic bins [35]. Furthermore, as explored by [35], large bin width conserves validity of the Limber equation and does not need for further corrections on border effects. Validity of such slicing is explored and  $\Delta z_s = 0.05$  is found to be adapted even for narrower tomographic bins than the ones used in the present work. It is also useful to express the angular two point correlation functions as a function of projected comoving transverse distance  $r_p$ , where  $r_p = \theta \chi(z)$  with the flat-sky approximation and at small angular scales. This is the transverse comoving distance at redshift  $z$  for a  $\theta$  angular separation, and is equal to the comoving distance if the curvature of the universe  $\Omega_k$  is null.

For this analysis, the same cosmological parameters as those used by HSC’s own clustering redshifts analysis [1] are used:  $\Omega_{\text{DM}} = 0.258868$ ,  $\Omega_b = 0.048252$ ,  $h = 0.6777$ ,  $n_s = 0.95$  and  $\sigma_8 = 0.8$ . For the rest of this work, angular separation will use the projected comoving distance  $r_p$  instead of  $\theta$  within this cosmology, where the redshift used to compute  $r_p$  is the

center of the spectroscopic bin used, noted  $z_j$  for a bin interval  $[z_j - \frac{\Delta z}{2}, z_j + \frac{\Delta z}{2}]$ <sup>5</sup>, with  $j$  the index of the bin. This now makes  $z$  a parameter for  $\omega_{x,y} = \omega_{x,y}(r_p, z)$ . Therefore, since  $r_p$  values and the dark matter autocorrelation function  $\xi_m$  used later in this analysis are computed in the context of the aforementioned cosmology, the results are cosmology dependent. With this in mind, we compute results for two scale cuts  $0.3 - 3h^{-1}\text{Mpc}$  and  $1 - 5h^{-1}\text{Mpc}$  and present results for both in section 6.

### 3.1 Density contrast

Focusing on the largest contribution term to the cross-correlation vector  $\mathbf{g} \times \mathbf{g}$ , one can write equation 3.4[33] with the Limber approximation [66]:

$$\begin{aligned} \omega_{x,y}^{\mathbf{g} \times \mathbf{g}}(r_p, z) &= \int b_x(z)n_x(z)b_y(z)n_y(z)\xi_m(r_p, z)dz \\ &\approx r_{xy}(r_p, z)\sqrt{\int b_x^2(z)n_x^2(z)\xi_m(r_p, z)dz \int b_y^2(z)n_y^2(z)\xi_m(r_p, z)dz} \\ &\approx r_{xy}(r_p, z)\sqrt{\omega_{x,x}^{\mathbf{g} \times \mathbf{g}}(r_p)\omega_{y,y}^{\mathbf{g} \times \mathbf{g}}(r_p)}, \end{aligned} \quad (3.4)$$

Here,  $\delta_x^{\mathbf{g}}(z, \theta) = b_x(z)\delta_m^{\mathbf{g}}(z, \theta)$  with  $b_x$  the galaxy-matter bias of sample  $x$ ,  $\delta_m^{\mathbf{g}}$  the 3D matter density,  $\xi_m(z, \theta)$  is the matter 3D two-point correlation function. Finally,  $r_{xy}(r_p, z)$  is the cross-correlation coefficient between the two galaxy samples, which is assumed to remain constant across redshift within a tomographic bin. This assumption is weaker than that of a linear galaxy bias, but is still expected to fail on very small scales. In the following sections, this work uses equation 3.4 over fine redshift bins. The validity of the Limber approximation [66] on fine redshift bins is explored in [39] and found to remain reasonable. Equation 3.4 is derived from the Cauchy-Schwarz inequality with the  $L^2$  norm where  $r_{xy}$  is the proportionality coefficient, here assumed to not evolve with redshift. The goal is to find an optimal compromise between the high signal to noise (SNR) obtainable at the very small angular clustering scales ( $\lesssim 0.5 h^{-1}\text{Mpc}$ ), and this modeling assumption that may be broken on small scales. Example cross-correlation measurements between the DR1 LRGs and the two first tomographic bins used in this analysis are showcased in figure 3.

### 3.2 Integrating over small-scales

Following similar notations to [35, 67], subscript  $s$  is used for the spectroscopic target class(es) and  $p$  for the photometric sample, replacing the generic  $x, y$  used previously (with  $x = y$  for auto-correlations).  $s$  can be any DESI tracer, such as BGS, LRG, ELG or QSO, or a combination of tracers. The photometric sample from HSC corresponding to the tomographic bin  $i$  is noted  $p_i$ , though in the remainder of this work  $p$  is often used to describe any tomographic bin. The target class selected on that redshift bin is noted  $s_j$ , and  $n_{s_j}(z) = n_s(z_j)$  are used interchangeably. The midpoint  $z_j$  is the fiducial redshift for that bin, useful for example to compute comoving scales.

Finally,  $\bar{\omega}_{xy}$  is the scale-averaged angular cross correlation vector, such that (in the case of cross-correlation between  $s_j$  and  $p_i$ ):

<sup>5</sup>For auto-correlations on the photometric dataset used in section 3.4, the distances are computed with the mid-point of the tomographic bin in mind.

$$\bar{\omega}_{s_j, p_i}(z_j) = \int_{r_{\min}}^{r_{\max}} W(r) \omega_{s_j, p_i}(r, z_j) dr \quad (3.5)$$

with  $W(r) \propto r^\beta$  the scale-dependent weighting function. In `pycorr`<sup>6</sup>, two-point correlation functions are expressed in terms of the fiducial angular separation  $\theta$ : the present work expresses bin edges defined with the transverse comoving distance  $r_p$ . For each narrow spectroscopic bin,  $r_p$  distances are computed with `astropy` [68] at the mid-point redshift  $z_j$ . This sets  $z_j$  as a parameter for  $\bar{\omega}$ . The weighting function  $W(r) = r^\beta / \int_{r_{\min}}^{r_{\max}} r^\beta dr$  is normalized to unity over integration scales, and  $\beta = -1$  is chosen following [29, 38]. This weighting function up-weights the smaller scales, where higher clustering signal is expected. Scale cut choices to apply to our correlation functions are represented by  $r_{\min}$  and  $r_{\max}$ . In literature, other weighting schemes have been explored, such as weighting directly the numerator and denominator of the two-point estimator (described in section 4), and integrating independently the numerator and denominator [30, 36, 38]. Alternative weighting schemes are not explored in this work. The fiducial scale cuts of this analysis are  $0.3 - 3h^{-1}\text{Mpc}$ : these cuts are more conservative than the cuts on the first clustering redshifts calibration [1],  $0.1 - 1\text{Mpc}$ . In section 6, we explore using an even more conservative scale cut ( $1 - 5h^{-1}\text{Mpc}$ ), and compare the results and error bars obtained.

### 3.3 Building the $n(z)$ model

For a single spectroscopic redshift bin (here, of size  $\Delta z_s = 0.05$ ), the  $n(z)$  distribution is assumed to be an indicator function of the redshift bin ( $n_x(z) = \mathbb{1}_{[z_j - \Delta z/2, z_j + \Delta z/2)}(z) / \Delta z$ ), constant over the redshift interval. One should note that this assumption holds well, except on the edge of the spectroscopic datasets where the  $N(z)$  drops, where it could induce slight biases. In the scope of this work, we decide to not investigate further this issue. Furthermore, neglecting the evolution of both galaxy biases as well as the evolution of the dark matter auto-correlation function over the spectroscopic redshift bin  $\Delta z_s$  leads to the Dirac approximation described in many clustering redshifts works [35, 36, 69], after integrating and weighting over small scales:

$$\bar{\omega}_{s_p}^{\text{g} \times \text{g}}(z_j) \approx n_p(z_j) b_s(z_j) b_p(z_j) \bar{\omega}_{mm}(z_j) \quad (3.6)$$

In particular, the galaxy bias for sample  $x$  can be obtained using the auto-correlations functions:  $\bar{\omega}_{x_x}^{\text{g} \times \text{g}}(z) \approx b_x(z)^2 \bar{\omega}_{mm}(z) / \Delta z$ . This means the spectroscopic galaxy bias is easy to recover, as the auto-correlation sample can be binned by true, spectroscopic redshift in bins  $s_j$ . The computation is performed for each of the DESI target classes, as described in section 4. However, such a measurement is not as easily obtained with photometric auto-correlations, as one cannot trust that the photometric redshifts lie on the defined bin interval. A correction needs to be applied to recover the photometric galaxy sample auto-correlations and approximate the galaxy bias redshift evolution: this process described in section 3.4. For now, if one assumes that the photometric redshifts are perfectly known, bins  $p_j$  of size  $\Delta z$  akin to the spectroscopic bins  $s_j$  can be used to probe the photometric bias evolution with equation 3.6. Assuming this, the  $n_p(z)$  model is:

$$n_p(z_j) \approx \frac{\bar{\omega}_{s_j p_j}^{\text{g} \times \text{g}}(z_j)}{\Delta z \sqrt{\bar{\omega}_{s_j s_j}^{\text{g} \times \text{g}}(z_j) \bar{\omega}_{p_j p_j}^{\text{g} \times \text{g}}(z_j)}} \quad (3.7)$$

---

<sup>6</sup>[github.com/cosmodesi/pycorr](https://github.com/cosmodesi/pycorr)

In equation 3.7, we neglect the redshift evolution of  $r_{x,y}$ . We further assume  $r_{x,y} = 1$  to simplify notations, as one can always re-normalize equation 3.7 later. In the following subsections, further systematic corrections to this expression are described. In Section 3.4, corrections to  $\bar{\omega}_{p_k p_k}$  are discussed in order to recover a proxy for the photometric galaxy bias, since one cannot obtain accurate  $p_k$  bins over photometric redshifts due to photo- $z$  scatter. In Section 3.5, second-order terms from magnification effects to the observed cross-correlation vector  $\bar{\omega}_{sp}$  are considered.

### 3.4 Galaxy bias for the photometric sample

In practice, the true redshifts of the photometric redshift distribution are not known. The photometric galaxy bias has to be taken into account in the  $n(z)$  model, but the scatter and potential outliers in each of the redshift bins does not allow us to accurately measure the auto-correlation of the photometric sample in small redshift bins  $\bar{\omega}_{p_k p_k}$ . Here,  $p_k$  is a smaller tomographic bin of width  $\Delta z_p = 0.1$  indexed by  $k$ : the binning is performed on the photometric redshifts. In this work,  $p_k$ 's are spread linearly from  $z_p \sim 0$  to  $z_p \sim 1.6$ : probing the galaxy bias further remains difficult due to the low number densities of QSO in higher redshift bins, without help from other tracers.

If the auto-correlation of the photometric tracer using the photometric redshift binning is noted  $\bar{\omega}_{pp}^{\text{photo}-z}$ , galaxy bias can be recovered by measuring  $\bar{\omega}_{pp}^{\text{true}}$ , that is, measured as if the sample was binned using true redshifts<sup>7</sup>. The correction employed in this study is close to previous works [33, 35, 36]. The correction is performed assuming the product of the photometric tracer galaxy bias with dark matter  $b_p(z)\sqrt{\bar{\omega}_{mm}(z)}$  is constant over  $p_k$  bins smaller than the fiducial tomographic bins, following [33]. A correction to  $\bar{\omega}_{pp}^{\text{photo}-z}$  is obtained by measuring  $n_{p_k}(z)$ , where  $n_{p_k}(z)$  is the clustering redshifts measurement of  $n(z)$  over the  $p_k$  tomographic bin and is obtained with equation 3.8:

$$n_{p_k}(z_j) \propto \frac{\bar{\omega}_{s,p_k}(z_j)}{\sqrt{\bar{\omega}_{ss}(z_j)}} \quad (3.8)$$

The above expression assumes constant photometric galaxy bias over the smaller tomographic bin, only correcting for the spectroscopic galaxy bias with auto-correlations in order to obtain the true redshift distribution, with  $\Delta z_p = 0.1$  as the small photometric redshift bin interval ranging  $z \sim 0$  to  $z \sim 1.6$ . While  $\Delta z_p = 0.1$  is not a small redshift interval for such an assumption, [35] explores the recovered bias expression differences with different bin sizes and finds similar corrections for  $\Delta z = 0.1$  and  $\Delta z = 0.02$ . We assess the validity of such an approximation in appendix A.

Since the photometric galaxy bias is assumed to be constant within these bins, the measured distributions are re-normalized and only implement the correction to the spectroscopic bias with  $\bar{\omega}_{ss}$ , as shown in equation 3.8.  $n_{p_k}(z)$  is measured with finer spectroscopic redshift bins ( $\Delta z_s = 0.025$ ) as finer tomographic bins need better redshift resolution in order to accurately recover the distributions. Dark matter evolution is also taken into account in the correction, following [35]: one obtains the following correction to the two-point correlation functions:

$$\bar{\omega}_{pp}^{\text{true}}(z_k) \approx \bar{\omega}_{pp}^{\text{photo}-z}(z_k) \frac{\Delta z_p^{-2} \int_{z_k - \Delta z_p/2}^{z_k + \Delta z_p/2} \bar{\omega}_{mm}(z) dz}{\int_0^\infty n_{p_k}^2(z) \bar{\omega}_{mm}(z) dz} \quad (3.9)$$

<sup>7</sup>Here, these notations are similar terminology to work done on the Dark Energy Survey clustering redshifts analyses [33]

Here,  $\bar{\omega}_{mm}(z)$  is the dark matter angular auto-correlation at redshift  $z$  over a  $\Delta z$  slice around  $z$ . Thus, equation 3.9 allows to approximate the correction to  $\bar{\omega}_{pp}^{\text{photo}-z}$ , therefore obtaining a proxy for the bias evolution in redshift of the photometric sample.

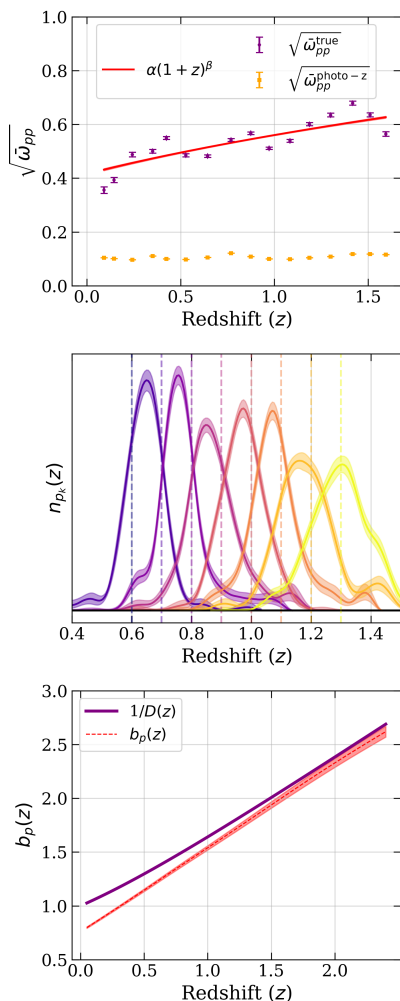


**Figure 4:** *Top panel:*  $\sqrt{\bar{\omega}_{pp}^{\text{true}}}$  and  $\sqrt{\bar{\omega}_{pp}^{\text{photo}-z}}$  with the power law fit through the corrected measurements. This showcases the importance of the correction, as the  $\sqrt{\bar{\omega}_{pp}^{\text{photo}-z}}$  alone does not capture significant galaxy bias evolution, whereas the correction captures a general evolution trend.

*Middle panel:* Clustering redshifts measurements for a few of the intermediate small tomographic bins ( $n_{p_k}(z)$  distributions), highlighting the tomographic bin ranges with the dotted lines. The  $n_{p_k}(z)$  are modeled with splines, described further in section 5.3. Nonetheless, the photometric redshift spread and the gradual expectation shift can be seen increasing with redshift, compared to the midpoint of the bins (between the dotted lines).

*Bottom panel:* Comparing  $b_p(z)$  computed with the corrections to  $\bar{\omega}_{pp}$  and a "passive evolution" galaxy sample where the linear bias follows  $b_p(z) \propto 1/D(z)$  with  $D(z)$  the growth factor of the universe.

The numerator of the correction corresponds to the influence of the spectroscopic redshift distribution over the tomographic bin, assumed to be flat. The denominator corrects for the photo- $z$  spread due to the chosen algorithm's inaccuracies, as the  $n_{p_k}(z)$  distribution cannot be assumed flat over the tomographic bin used. The square root of these corrected auto-correlations is fit to a power-law model (see Figure 4), as done in works from DES<sup>8</sup> [30, 33], and the fitting errors are propagated to the  $p(z)$  measurements.

$$\sqrt{\bar{\omega}_{pp}^{\text{true}}} \approx \alpha(1+z)^\beta \quad (3.10)$$

The fit gives  $\alpha = 0.416 \pm 0.004$  and  $\beta = 0.430 \pm 0.0145$  for the chosen scale cut  $0.3 - 3 h^{-1} \text{Mpc}$ . Values are fit on the expectations of the small tomographic bins. In figure 4, the measurements of galaxy bias and the power law approximation are shown in the left panel, as well as the

<sup>8</sup>This analysis includes a free amplitude parameter  $\alpha$  in the fit. Though normalization allows one to drop the amplitude term, the error is still included in error propagation.

clustering redshifts measurements for a few of the intermediate tomographic bins used to compute the corrections and characterize the local photo- $z$  spread in the middle panel. In the right panel, the bias evolution of the photometric sample  $b_p(z)$  is computed using the dark matter auto-correlation and compared to a passive evolution type sample that would follow  $b(z) \propto 1/D(z)$  where  $D(z)$  is the (cosmology-dependent) normalized factor of growth. With this correction, the HSC sample bias evolution is slightly faster than the factor of growth but still comparable. This observed behavior is consistent with measurements of the large-scale galaxy bias of HSC Year 1 [70], where proportionality  $b(z) \propto 1/D(z)$  is observed for flux-limited samples.

### 3.5 Magnification

In this subsection, the impact of second order terms ( $g \times \mu$  and  $\mu \times g$ ) due to magnification effects are described and modeled. Magnification arises via weak lensing effect, which can magnify or de-magnify galaxy flux, depending on the slope of the luminosity function. This (de)magnification is caused by matter distribution along the line of sight, which is correlated with the galaxy distribution at lower redshifts. In turn this introduces non-zero correlation between high redshift galaxies and low redshift galaxies. The total observed flux of individual galaxies increase caused by magnification affects both the selection function of galaxies [71] and the photometric redshift algorithm, since both rely on the observed properties of the sample. These biases are dominant when cross-correlating sources that are far apart in redshift. Magnification effects for auto-correlations are neglected. Magnification bias effects are described with the log-number count slope, characterizing the effects on the observed projected number density:

$$s_\mu = \frac{d \log_{10} N(> m)}{dm} \quad (3.11)$$

where  $m$  is the limiting magnitude of the sample, and  $N$  is the cumulative number count as a function of limiting magnitude. In practice,  $s_\mu$  is a partial derivative, since  $N(> m)$  depends on other selection effects such as redshift binning depending on the sample [70]. DESI tracers often have complex selection functions [49–52] and therefore cannot be characterized by a simple magnitude cut. A common technique to probe the magnification bias in that case, used for example when computing the LRG magnification bias [72], is to shift the magnitudes in all bands by a small amount  $\delta m$  and measure the response on  $s_\mu$  after reapplying target selection, going cut by cut. The magnification bias can then be written as  $\alpha_x = 2.5s_\mu - 1$  [30, 32]<sup>9</sup>, where  $x$  denotes a galaxy sample, either spectroscopic or photometric.

The formalism developed in works like [64] and used in [31–33, 35] is adopted to model the magnification correction on the cross-correlation vectors. The correction is theoretically obtained using the following:

$$W_x^\mu(\chi) = \frac{3\Omega_m H_0^2}{2c^2} \int_\chi^\infty n_x(\chi') \frac{\chi}{a(\chi)} \frac{\chi' - \chi}{\chi'} d\chi' \quad \text{and} \quad W_x^g(\chi) = n_x(z) \frac{dz}{d\chi}(\chi) \quad (3.12)$$

where  $W_x^\mu(\chi)$  is the tomographic lens efficiency of sample  $x$  and  $W_x^g(\chi)$  is the selection function of galaxies in the redshift bin. The expression of the angular cross power-spectrum between fields A, B with the Limber approximation [66] gives:

---

<sup>9</sup>Other parametrizations are common, such as  $\alpha = 2.5s_\mu$  [72–74], or  $\alpha = \left. \frac{d \ln(f_1)}{dm} \right|_m$  [75], where  $f_1$  is the fraction of galaxies passing the cut.

$$C_{s_j p_i}^{\text{AB}}(\ell) = \int \frac{W_{s_j}^{\text{A}}(\chi) W_{p_i}^{\text{B}}(\chi)}{\chi^2} P_{\text{AB}} \left( k = \frac{\ell + 0.5}{\chi}, z(\chi) \right) d\chi \quad (3.13)$$

and the angular power spectra can be converted into angular correlation functions through a Legendre transformation. Here,  $P_{\text{AB}}$  is the corresponding 3D power spectrum model for fields A,B. More in-depth demonstrations can be found in works [33, 35]. The following expression per tomographic bin  $p$  and target class  $s$ , as demonstrated in Appendix B of [35], is obtained:

$$\bar{M}(z_j) = \alpha_s(z_j) \sum_{i < j} b_p(z_i) n_p(z_i) \mathcal{D}(z_i, z_j) + b_s(z_j) \sum_{i > j} \alpha_p(z_i) n_p(z_i) \mathcal{D}(z_j, z_i) \quad (3.14)$$

with  $\mathcal{D}(z_x, z_y)$  defined as:

$$\mathcal{D}(z_x, z_y) := \frac{3H_0^2 \Omega_m}{c} \frac{\bar{\omega}_m(z_j) \Delta z}{H(z_x) a(z_x)} \frac{\chi(z_y) - \chi(z_x)}{\chi(z_y)} \chi(z_x) \quad (3.15)$$

In the above expression,  $H$  is the Hubble parameter,  $H_0 = H(z = 0)$ ,  $\chi$  is the comoving radial distance,  $c$  is the speed of light and  $a(z) = 1/(1+z)$  is the scale factor of the universe. Our expression differs slightly from [33] (like [35], redshift evolution of  $\alpha_s, \alpha_p, b_s, b_p$  is included, though for  $\alpha_p$  it will be neglected) and is closer to [35], the only difference being that the expression is averaged over comoving scales, removing dependencies on angular variables. The non-linear 2D angular matter power spectrum  $\bar{\omega}_{\text{mm}}(z_j)$  (on a  $\Delta z$  redshift slice around  $z_j$ ) is obtained using **Core Cosmology Library (CCL)**<sup>10</sup> [76] with the same fiducial cosmology as previously described and used in HSC's own clustering redshift analysis [1], reminded earlier in section 3. The matter power spectrum is predicted and computed with models from **halofit** [77] and **CLASS**<sup>11</sup> [78], and any computation of the matter power spectrum in this work uses these predictions. The real space contribution is then computed with the Legendre series transform. Because magnification corrections on the auto correlations are neglected, the magnification correction is a linear system to solve  $\mathcal{M}\mathbf{X} = \mathbf{n}$  where  $\mathbf{n}$  is the measurement vector,  $\mathbf{X} = (n_p(z_j))_{j \in \llbracket 1, N_b \rrbracket}$  are the magnification-corrected measurements,  $N_b$  is the number of bins and  $\mathcal{M}$  is a "magnification matrix" such that:

$$\mathcal{M} = (m_{kl})_{k,l \in \llbracket 1, N_b \rrbracket} = \begin{cases} \frac{1}{\Delta z \sqrt{\bar{\omega}_{s_k s_k} \bar{\omega}_{p_k p_k}}} \alpha_s(z_k) b_p(z_l) \mathcal{D}(z_l, z_k) & \text{if } k < l \text{ (g} \times \mu\text{)} \\ 1 & \text{if } k = l \text{ (g} \times \text{g)} \\ \frac{1}{\Delta z \sqrt{\bar{\omega}_{s_k s_k} \bar{\omega}_{p_k p_k}}} \alpha_p(z_l) b_s(z_k) \mathcal{D}(z_k, z_l) & \text{if } l > k \text{ (\mu} \times \text{g)} \end{cases} \quad (3.16)$$

The measurement vector  $\mathbf{n}$  is:

$$\mathbf{n} = \left( \frac{\bar{\omega}_{s_j p_i}}{\Delta z \sqrt{\bar{\omega}_{p_j p_j} \bar{\omega}_{s_j s_j}}} \right)_{j \in \llbracket 1, N_b \rrbracket} \quad (3.17)$$

In parentheses of equation 3.16, contributions from different effects in the matrix are highlighted. The dominant term is by far the diagonal term, corresponding to the galaxy density contribution  $\text{g} \times \text{g}$ .

<sup>10</sup>[github.com/LSSTDESC/CCL](https://github.com/LSSTDESC/CCL)

<sup>11</sup>[github.com/lesgourg/class\\_public](https://github.com/lesgourg/class_public)

The galaxy bias expressions can be obtained through auto-correlations, as detailed in section 3.3. For the photometric tracer, the power law approximation described in section 3.4 is adopted to recover the bias expression, after computing the dark matter auto-correlation. Therefore, the matrix coefficients become:

$$m_{kl} = \begin{cases} \frac{b_p(z_l)\alpha_s(z_k)}{b_p(z_k)b_s(z_k)\bar{\omega}_{mm}(z_k)}\mathcal{D}(z_l, z_k) & \text{if } k < l \\ 1 & \text{if } k = l \\ \frac{\alpha_p(z_l)}{b_p(z_k)\bar{\omega}_{mm}(z_k)}\mathcal{D}(z_k, z_l) & \text{if } k > l \end{cases} \quad (3.18)$$

The magnification corrected measurements are obtained with  $\mathbf{X} = (n_p(z_j))_{j \in [1, N_b]}$  and the error bars are propagated assuming:

$$\mathcal{M}(X + \delta X) = (\mathbf{n} + \delta \mathbf{n}) \Rightarrow \delta X = \mathcal{M}^{-1} \delta \mathbf{n} \quad (3.19)$$

Magnification bias and galaxy bias measurements are not marginalized over further, given the amplitude of the correction with respect to measurements. In the data products of this work, distributions and measurements with and without this correction are included.

The next paragraphs describe the galaxy bias and magnification bias measurements used in the context of this analysis for our magnification correction.

**Galaxy bias** For the spectroscopic sample, the galaxy bias used to correct for magnification effects is measured using auto-correlation measurements on the spectroscopic tracer. To model the galaxy bias of any spectroscopic tracer, the parametrization introduced by [79], and also used by [80] is implemented:

$$b_s(z) = c_s(1+z)^2 + d_s \quad (3.20)$$

The linear galaxy bias is obtained with the monopole of the auto-correlation functions, with the technique described in [80]. Measurements are fit to each of the target classes<sup>12</sup> between scales of 30 to 65h<sup>-1</sup>Mpc with the DESI fiducial cosmology (described in, for example, [81]). While one could use the existing auto-correlation functions to measure linear galaxy bias in the magnification correction, a more robust bias measurement that overcomes small-scale nonlinearities and projection effects is obtained by measuring the 3D auto-correlation on larger scales. Nonetheless, the galaxy bias measurements obtained with the small scale angular auto-correlations are consistent with the larger scale measurements. The fitted parameters are given in the following Table 2.

For the photometric sample galaxy bias, the fitted power-law described in 3.4 as correction to  $\sqrt{\bar{\omega}_{pp}^{\text{photo}-z}}$  can be used to recover the expression of  $b_p(z)$  at all redshifts using the power-law fit.

**Magnification bias** The number count slope  $s_\mu$  and magnification bias  $\alpha_x$  were introduced in section earlier 3.5. For HSC, the magnitude cut  $i_{\text{band}} - a_i < 24.5$  is considered to be the dominant selection function in HSC, where  $i_{\text{band}}$  is the HSC i-band `cModel` magnitude<sup>13</sup>, and  $a_i$  is the absorption for  $i$  band. Magnification slope coefficients for HSC are assumed constant

<sup>12</sup>The measurement of the galaxy bias for BGS is performed on the `BGS_BRIGHT-21.35` sample. More details about this selection can be found in the DESI DR2 Baryon Acoustic Oscillation (BAO) work [53]. The linear galaxy bias difference between the two samples (`BGS_ANY` and `BGS_BRIGHT-21.35`) is assumed to be negligible in the context of the magnification correction.

<sup>13</sup>Details on the HSC `cModel` magnitudes can be found in sub-subsection 4.9.9 of [82].

**Table 2:** Galaxy bias model coefficients fitted to the DR2 two-point auto-correlation functions, within the DESI fiducial cosmology presented in [81] and reduced  $\chi^2$  statistic of the fit. The coefficients are assumed to be the same for DR1.

Tracer	$c_s$	$d_s$	$\chi_r^2$
BGS	$0.606 \pm 0.073$	$0.524 \pm 0.129$	0.59
LRG	$0.236 \pm 0.019$	$1.346 \pm 0.058$	1.39
ELG	$0.155 \pm 0.012$	$0.595 \pm 0.057$	1.53
QSO	$0.252 \pm 0.008$	$0.710 \pm 0.058$	1.62

per tomographic bin. Tomographic bins are affected by two significant selections that could alter the magnification slope: the calibration cut, detailed in section 2.2 for the first two tomographic bins, and the selection based on binning with photometric redshifts. In a HSC Y1 analysis performed in [70], only the magnitude selection was considered, hence the same assumption is kept. Following the approach described in that work to estimate  $s_\mu$ , a fourth order polynomial is fit to the cumulative number counts. The polynomial is then derived, log-scaled and evaluated at the limiting magnitude to obtain  $s_\mu$ . Measurements can be found in the following table 3.

**Table 3:** Magnification bias for each tomographic bin. Redshift evolution within tomographic bins is neglected.

Tomographic bin	$s_\mu$
Bin 1 ( $z : 0.3 - 0.6$ )	0.002
Bin 2 ( $z : 0.6 - 0.9$ )	0.065
Bin 3 ( $z : 0.9 - 1.2$ )	0.142
Bin 4 ( $z : 1.2 - 1.5$ )	0.206

In the case of the DESI dataset, magnification measurements are obtained from literature [72, 83, 84] as well as from measurements performed with the same methodology as [75] for ELGs. For ELGs, it is assumed that ELG-LOP and ELG-LOP+VL0 have the same magnification bias (combined under the ELG tag), computed exclusively on the ELG-LOP target class<sup>14</sup>. The magnification biases are compiled under table 4.

Magnification biases are linearly interpolated with these measurements, following choices made by works in DES [32] (for example for the redMaGiC sample). In order to be accurate, magnification biases would require a single measurement per spectroscopic bin  $j$ , but given the amplitude of the correction with respect to the  $g \times g$  contribution, interpolation is assumed to be negligible within this correction.

## 4 Computing the two-point angular functions

Two point angular correlations are computed with the `pycorr` software, based on the `CORRFUNC`<sup>15</sup> [85, 86] engine. HSC and DESI’s survey footprints are extracted using multi-order coverage

<sup>14</sup>The largest bias from ELG magnification effects is on Bin 3’s high redshift tail. This happens at the higher redshift range of ELGs ( $z \gtrsim 1.1$ ), where there are significantly less ELGs from ELG-VL0, as shown in Figure 2.

<sup>15</sup>[github.com/manodeep/Corrfunc](https://github.com/manodeep/Corrfunc)

**Table 4:** Magnification slope for each tracer and effective redshift. For LRGs, the provided  $\bar{z}$  redshifts are the mid-point redshift of the photometric redshift bins used to compute the magnification coefficient. The effect of photo- $z$  bias or scatter is not considered further in the measurement.

Tracer	$s_\mu$	$\bar{z}$
BGS [83]	0.81	0.211
	0.80	0.352
LRG [72]	$0.954 \pm 0.027$	0.44
	$0.988 \pm 0.025$	0.51
	$1.040 \pm 0.021$	0.59
	$1.047 \pm 0.018$	0.67
	$0.999 \pm 0.021$	0.75
	$0.957 \pm 0.017$	0.82
	$0.914 \pm 0.018$	0.89
	$1.078 \pm 0.020$	0.97
ELG	$0.546 \pm 0.005$	0.95
	$0.666 \pm 0.005$	1.35
QSO [84]	0.099	1.44
	0.185	2.27
	0.284	2.75

maps (MOC) [87] made with the `mocpy`<sup>16</sup> python package. The areas of interest for this study represent the intersection of DESI’s MOC with HSC’s MOC. The computations of the two-point angular functions are split up into four patches of sky, corresponding to spatially close areas, in order to speed up computing time. Concretely, this corresponds to the XMM field, the HECTOMAP field, the VVDS field, and the joint field composed of GAMA09H, GAMA15H and WIDE12H. We use  $N_b = 32$  logarithmically-spaced angular bins, with edges spanning  $0.1$  to  $10 \text{ h}^{-1}\text{Mpc}$ , in transverse comoving scales.

The DESI angular auto-correlations are obtained by combining the auto-correlation measured in the north galactic cap (NGC) and south galactic cap (SGC) of the dataset used. Two point correlation functions are computed independently per DESI tracer, and include standard weights and the FKP weights [88]. The weighting used is described in [59]:  $w_{\text{tot}} = w_{\text{comp}}w_{\text{sys}}w_{\text{zfail}}w_{\text{FKP}}$ . Here,  $w_{\text{comp}}$  is used for completeness,  $w_{\text{sys}}$  accounts for target density fluctuations due to imaging conditions and  $w_{\text{zfail}}$  encompasses the relative redshift success rate. Given the redshift ranges used in this analysis, the FKP weights  $w_{\text{FKP}}$  are not strictly necessary, since their purpose is to describe how the number density changes with redshift, and the redshift bins are fine. It is important to note that fiber assignment incompleteness affects our measurements on these small scales, especially for low completeness tracers such as ELGs. This effect is all the more prominent for DR1 ELGs, which is why we decide to not use them in this analysis. In short, the number of targets who obtain a fiber on a single DESI tile while observing is different from the total number of possible targets in that target class within the tile. To mitigate this effect, one could use Pairwise Inverse Probability (PIP, [89]) weights when computing two point correlation functions, but this is only doable when performing auto-correlations. Since cross-correlations are performed with

<sup>16</sup>[github.com/cds-astro/mocpy](https://github.com/cds-astro/mocpy)

the HSC catalog, PIP weighting is not available, though it is noteworthy that most of HSC's footprint is already within DESI areas with high or maximal completeness, as shown in figure 1. This kind of clustering redshift study will benefit from subsequent data releases of DESI, alleviating further this issue. To verify this introduces no apparent bias in the measurements, two scale cuts are included in this work:  $0.3 - 3h^{-1}\text{Mpc}$  and  $1 - 5h^{-1}\text{Mpc}$ . The fiber collisions become an issue below  $\theta_{\text{fib}} = 0.05^\circ$  [90, 91]. The second scale cut allows for no leakage of fiber collisions in the scale cut up to  $z \sim 0.45$ , with minor contamination for larger redshifts. The measurement consistency shown in section 6 supports that no bias is introduced by using measurements at smaller scales.

With the HSC catalog, the lensing weights are included in our two-point estimators, following the same choices as [1]. Jackknife estimates of the covariance matrix are computed to estimate error bars, including the correction given by [92], which is the fiducial approach implemented in `pycorr`. Per patch of the sky,  $N_{\text{JK}} = 100$  "delete-one" jackknife realizations are performed: in each iteration, a random area of sky in the footprint is removed and the two-point angular statistic is computed with that area excluded. Removed areas are determined through a KMeans sub-sampler algorithm splitting up the footprint into  $N_{\text{JK}}$  areas at `HEALPix` [93] nside resolution of 256 on each of the patches of sky. The covariance matrix obtained on the associated angular two-point correlation functions can be written as such [92]:

$$\mathbf{C}_{ij} = \frac{N_{\text{JK}} - 1}{N_{\text{JK}}} \sum_{n=1}^{N_{\text{JK}}} (\omega_i^{(n)} - \langle \omega_i \rangle) (\omega_j^{(n)} - \langle \omega_j \rangle) \quad (4.1)$$

where  $(N_{\text{JK}} - 1)/N_{\text{JK}}$  is the fraction of the footprint's area used to compute any jackknife realization,  $\omega_i^{(n)}$  is the measurement in angular bin  $i \in \llbracket 1, N_b \rrbracket$  over the footprint excluding area  $n$  and  $\langle \omega_i \rangle$  is the mean value over all measurements in bin  $i$  from excluded regions. The Davis-Peebles [94] estimator is chosen to compute the two-point angular correlation functions:

$$\hat{\omega}_{xy}(r) := \frac{D_x D_y(r)}{R_x D_y(r)} - 1 \quad (4.2)$$

where  $D_x D_y$  are normalized data-data pair counts and  $D_x R_y$  are the normalized data-random pair counts. Although this estimator is not as low bias and variance as the broadly used Landy-Szalay [95] estimator:

$$\hat{\omega}_{xy}^{\text{LS}}(r) := \frac{D_x D_y(r) - R_x D_y(r) - D_x R_y(r)}{R_x R_y(r)} + 1, \quad (4.3)$$

the Davis-Peebles estimator allows this study to not rely on the random catalog of the photometric sample, and only rely on the random catalog for our spectroscopic tracers. A random catalog for HSC is still used when computing the auto-correlations on smaller tomographic bins  $\bar{\omega}_{pp}^{\text{photo}-z}$ , in the context of photometric galaxy bias mitigation (see section 3.4). This random catalog has no redshift assignments, so it is less robust than the DESI catalog, but captures the footprint sufficiently well given our measurement.<sup>17</sup> Conveniently, the Davis-Peebles estimator is also faster to compute. At least 10 times more randoms

<sup>17</sup>More details about the random points used can be found on the HSC data release 3 portal: [hsc-release.mtk.nao.ac.jp/random-points\\_\\_pdr3/](https://hsc-release.mtk.nao.ac.jp/random-points__pdr3/).

from the DESI catalogs than data points are used when computing the two-point correlation functions<sup>18</sup>, and for low-density datasets such as QSOs, this can reach up to 100 times more.

## 5 Parametrization methods

This section presents our parametrization choices for the tomographic redshift distributions for each bin. The benefit of such modeling is to regularize and smooth out the  $n(z)$  distributions, as some measurements statistically fluctuate to negative values. We compare some literature approaches, and introduce a new parametrization based on splines. The hierarchical Bayesian method proposed in [1, 96] leveraging both the **PhotZ** (photometry calibration) and **WX** (clustering redshifts measurements) distributions is not implemented, due to inconsistencies between the two calibrations: we therefore rely only on the clustering redshift measurements.

### 5.1 Combining tracers

Before parameterizing, once the  $n(z)$  for each target class is measured and, if necessary, corrected for other systematic effects such as magnification or galaxy bias, only target classes with significant overlap with the bin signal are retained. As such, Bin 1 ( $z \sim 0.3 - 0.6$ ) uses measurements from the BGS, LRGs and ELG-LOP. Bin 2 ( $z \sim 0.6 - 0.9$ ) uses every target class available, including QSOs. In Bin 3 ( $z \sim 0.9 - 1.2$ ) and Bin 4 ( $z \sim 1.2 - 1.5$ ), BGS derived constraints are removed as they present no significant overlap in redshift. Still, cross-correlations between all tracers and the tomographic bins are computed to assert consistency will null measurements on the redshift ranges of excluded tracers<sup>19</sup>. For each bin, after combining results, the measurements are restricted to the following ranges: in Bin 1, the model is retained between  $z \sim 0$  and  $0.8$ ; in Bin 2, between  $z \sim 0.3$  and  $1.3$ ; in Bin 3, between  $z \sim 0.3$  and  $2.1$ ; and in Bin 4, between  $z \sim 0.7$  and  $2.1$ . Once the measurements for each necessary target class within a single tomographic bin are obtained, the target classes are combined into a single measurement using inverse variance weighting<sup>20</sup>:

$$n(z_j) = \left( \sum_{t \in \mathcal{T}_j} \frac{1}{\sigma_t^2} \right)^{-1} \sum_{t \in \mathcal{T}_j} \frac{n_t(z_j)}{\sigma_t^2} \pm \sqrt{\left( \sum_{t \in \mathcal{T}_j} \frac{1}{\sigma_t^2} \right)^{-1}} \quad \forall j \in \llbracket 1, N_b \rrbracket \quad (5.1)$$

where  $\mathcal{T}_j$  is the set of target classes used at redshift  $z_j$ ,  $n_t(z_j)$  is the measurement of  $n(z)$  derived from target class  $t$  at redshift  $z_j$  with the associated error  $\sigma_t$ . Cross-covariance effects between tracers on overlapping spectroscopic redshifts are not taken into account. This ultimately affects our measurements with some over-confidence on multi-target redshift ranges (for example, between  $z \sim 0.7$  and  $z \sim 1.2$ , ELGs, LRGs and QSOs overlap and are

<sup>18</sup>This corresponds to four catalogs of randoms from the Large Scale Structure catalogs of DESI [59]. Each catalog corresponds to a number density of  $2500 \text{ deg}^{-2}$ , so the random catalog number density is  $10000 \text{ deg}^{-2}$  before redshift binning.

<sup>19</sup>When performing clustering redshifts measurements on smaller tomographic bins of width  $\Delta z_p$  centered on  $z_k$  while correcting for sample galaxy bias (see 3.4), we use the available tracers in bins of centers included in  $[z_k - 3\Delta z_p, z_k + 3\Delta z_p]$  per tomographic bin  $k$ . Bin  $z \sim 0. - 0.025$  is not taken into account due to very low densities (as reported by Figure 2 for the HSC sample) and high variance biasing the spline model

<sup>20</sup>When combining measurements if retaining only the cross-correlations (without correcting for auto-correlations), the measurements are combined on the two-point correlation counts themselves instead, due to normalization differences between target classes because of the amplitude of the auto-correlations. Hence, the samples are treated as a single "combined" target class.

all used in the analysis): this is not modeled further in the context of this work and could be improved upon in future works.

## 5.2 Suppressed Gaussian Processes

A recently developed approach introduced and implemented in Euclid methodological analyses for clustering redshifts [35, 67] involves using gaussian processes that are then suppressed in order to model measurements in a non-parametric way. In short, the data is modeled using Gaussian Processes (GP) with a Matérn kernel, setting a slope of  $\nu_{\text{GP}} = 1.5$  and a fixed length scale  $l_{\text{GP}} = \Delta z$ . In this work, GPs are implemented using `scikit-learn`<sup>21</sup> [97] and the suppression function proposed in [35, 67], varying the damping factor. The suppression function implemented depends on  $x$ , the convolution of a gaussian window with the local Signal to Noise Ratio (SNR) of the measurements, and a dampening factor  $k$ . The suppression function is as follows:

$$S(x, k) = \begin{cases} 0 & \text{if } x < 0 \\ 1 - (1 - x)^k & \text{if } 0 < x < 1, \\ 1 & \text{if } x > 1. \end{cases} \quad (5.2)$$

Such a suppression function tends to suppress real, tail like effects in large tomographic bins with important scatter. This is not as worrisome for experiments like LSST, expecting narrower tomographic bins, but poses issues with tomographic bins in other weak lensing surveys such as HSC (the concerning bin being Bin 3 with a long, high-redshift tail, for example) [1] or DES (for example, Bin 4) [32] that are spread out. Fine-tuning the suppression function could be an option to explore in order to correctly use the suppressed gaussian processes model, but is not explored further in the scope of this paper.

## 5.3 B-spline parametrization

The  $n(z)$  distributions are modeled with univariate basis splines (B-splines) over the redshift range. B-splines are families  $(B_i)_{i \in [1, n]}$  of piece-wise polynomials of order  $k \geq 1$ , with  $p = k - 1$  being the degree of the polynomials. These are defined by a sequence of knots  $t_0 \leq t_1 \leq \dots \leq t_m$ , with knots  $t_0, \dots, t_p$  and  $t_{m-p}, \dots, t_m$  known as external knots, usually repeated in order to support the first and last B-splines of the basis. The other knots lie on the range one is interested in and are known as internal knots. Knots will now refer to the internal knots. B-splines are defined by recursion using the Cox-de Boor formula:

$$\forall p \in \mathbb{N} \quad B_{i,p}(z) := \begin{cases} \mathbb{1}_{[t_i, t_{i+1})}(z) & \text{if } p = 0, \\ \frac{z - t_i}{t_{i+p} - t_i} B_{i,p-1}(z) + \frac{t_{i+p+1} - z}{t_{i+p+1} - t_{i+1}} B_{i+1,p-1}(z). & \text{if } p > 1 \end{cases} \quad (5.3)$$

where  $\mathbb{1}_{[t_i, t_{i+1})}$  is the indicator function of  $[t_i, t_{i+1})$ , null when  $z \notin [t_i, t_{i+1}[$  or if  $t_i = t_{i+1}$ . B-splines are by construction non-negative, and an example basis for the distribution in Bin 2 is shown in the bottom left panel of figure 5. For this model, one can use M-splines, where  $B_{i,p}(z)$  are normalized to integrate to 1: such a change only affects the prior of the normalization factor  $A$  described in the following model 5.4. To obtain our  $n(z)$  distributions with  $\hat{n}(z)$ ,  $\hat{n}(z)$  is parametrized as a function of our B-spline basis  $(B_{i,p})_{i \in [1, m]}$ ,

<sup>21</sup>[github.com/scikit-learn/scikit-learn](https://github.com/scikit-learn/scikit-learn)

free coefficients  $(c_i)_{i \in \llbracket 1, m \rrbracket}$ , and a free amplitude parameter  $A$  to account for re-normalization. Therefore:

$$\hat{n}(z) = A \sum_{i=1}^m c_i B_{i,p}(z) \quad (5.4)$$

The  $c_i$  coefficients are subject to a Dirichlet prior  $\mathbf{Dir}(\boldsymbol{\alpha})$ , which implies the  $c_i$  coefficients lie on the standard  $m - 1$  simplex: that is,  $\sum_{i=1}^m c_i = 1$  and  $c_i \in [0, 1]$  for all  $i \in \llbracket 1, m \rrbracket$ .

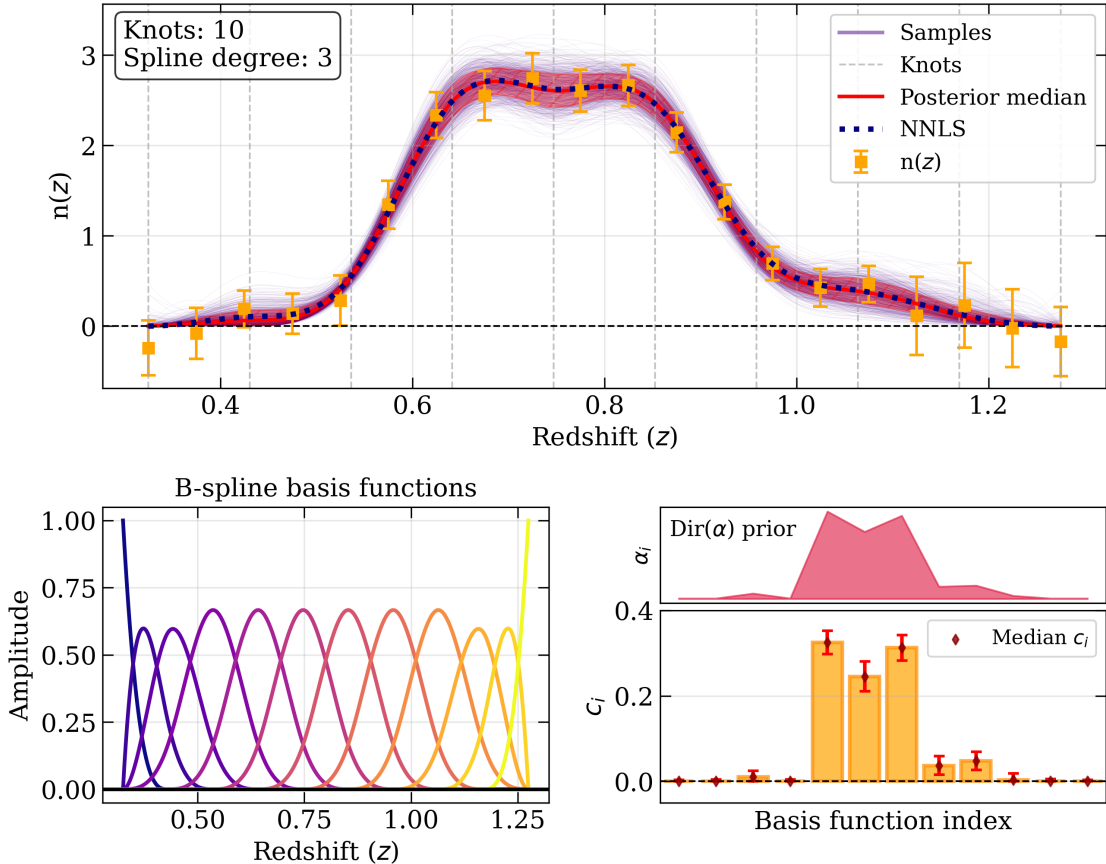


**Figure 5:** *Top panel:* Bin 2 data (as presented in section 6 with all corrections) overlaid with the spline distribution (red, posterior median and  $1\sigma$  contour) and some example samples from the spline modeling (indigo). Position of interior knots are shown in gray dotted lines. The NNLS result of equation 5.4 is shown in dashed navy. *Bottom left panel:* B-spline functions  $(B_i)_{i \in \llbracket 1, n \rrbracket}$  over the redshift range. *Bottom right panel:* In the bottom plot, we show the posterior median coefficient distribution over the samples with associated standard deviations, where  $c_i$  coefficients are constrained to be positive. Above, the  $\mathbf{Dir}(\boldsymbol{\alpha})$  prior is showcased, per expression 5.5.

In order to refine this prior, prior concentrations defined by the  $\boldsymbol{\alpha}$  vector on the  $c_i$ 's are adapted to encourage these coefficients to use values closer to 0 where the measurements are consistent with 0 (that is, where the cross-correlation signal is consistent with 0, modulo statistical fluctuations), which means little to no contribution from that spline function in the basis. Such refinement of the  $\boldsymbol{\alpha}$  vector is guessed by solving Non-Negative Least Squares

(NNLS) using equation 5.4 against the  $n(z)$  measurements (and fixing  $A$  to 1), obtaining coefficients  $c_i^{(\text{NNLS})}$ . When solving NNLS in this scenario, varying errors for each measurements are not taken into account, and results are only used as a guess for the prior. Two hyperparameters are defined to tune this prior: the base  $a_0$  being the minimal prior concentration to ensure sampling of the Bayesian model and a boost factor  $b$  that controls the local prior concentration. Therefore:

$$\alpha_i = a_0 + bc_i^{(\text{NNLS})} \quad \forall i \in \llbracket 1, m \rrbracket \quad (5.5)$$

This analysis chose  $b = 3$  and  $a_0 = 0.05$ . The prior  $\mathbf{Dir}(\boldsymbol{\alpha})$  set on Bin 2 of the tomographic bins is given as example in Figure 5 in the bottom right panel. The knots are uniformly distributed on the redshift grid with one knot every two data points: their positions are shown in dashed gray in figure 5. The free amplitude coefficient is subject to a broad gaussian prior over the initial amplitude  $A_0$  parameter computed with NNLS, with a standard deviation of  $0.25A_0$ . The spline models are obtained with Bayesian analysis using the software package `pymc`<sup>22</sup> [98].

## 6 Results

This section presents the calibrated  $n(z)$  distributions and the expectations we measure on each of the tomographic Bins. The measurements of this work are put in context of the previous clustering redshift analysis [1] on the HSC dataset, as well as the cosmic shear results [8, 9], cosmic shear ratios (CSR) calibration [57] and the combination of galaxy clustering with weak lensing (GC-WL) measurements [58] of the photometric redshift shifts. Redshift expectation values are measured as the first moment of the posterior draws from the spline model described in section 5 for each Bin. The resulting expectation value for each draw is split into 16<sup>th</sup>, 50<sup>th</sup> and 84<sup>th</sup> percentiles in order to obtain error measurements and the center expectation value.

The impact of the successive corrections made to the clustering redshifts measurements are shown with Bin 1 as an example in the upper panel of Figure 6. Similar global shifts are observed on every tomographic Bin due to the successive corrections. In the lower panel of Figure 6, measurements with all corrections and the associated spline models are shown. For comparison, we replicate the **PhotZ** photometry calibrated distributions presented in Figure 8 of [1].  $\Delta z$  "shift" values are reported in Table 5 and displayed in Figure 7. These shifts are measured as a difference of mean values with respect to the reported Y3 Total distribution means obtained in [1]. Per convention, a negative shift implies the considered measurement has a preference for a higher expectation value compared to the Y3 Total measurement.

The shift parameter results offer competitive measurements exclusively from clustering redshifts, as showcased in Figure 7. In this work, we follow the recommendations from the first HSC analysis (see notes (iv) and (v) of Section 7 from [1]), by modeling the evolution of the galaxy-dark matter bias for both the photometric sample and the spectroscopic sample, as well as corrections due to magnification effects. Moreover, the calibration sample we use here has redshifts  $z \gtrsim 1.2$  with QSO and ELG sources, allowing for complete calibration of Bin 3 and Bin 4, and the calibration sample is entirely composed of spectroscopic redshifts.

As such, in the upper panel of Figure 6, we can notice the relative impact of each of the calibrations on tomographic Bin 1. This work hints at biases in Bin 1 calibration,

---

<sup>22</sup>[github.com/pymc-devs/pymc](https://github.com/pymc-devs/pymc)

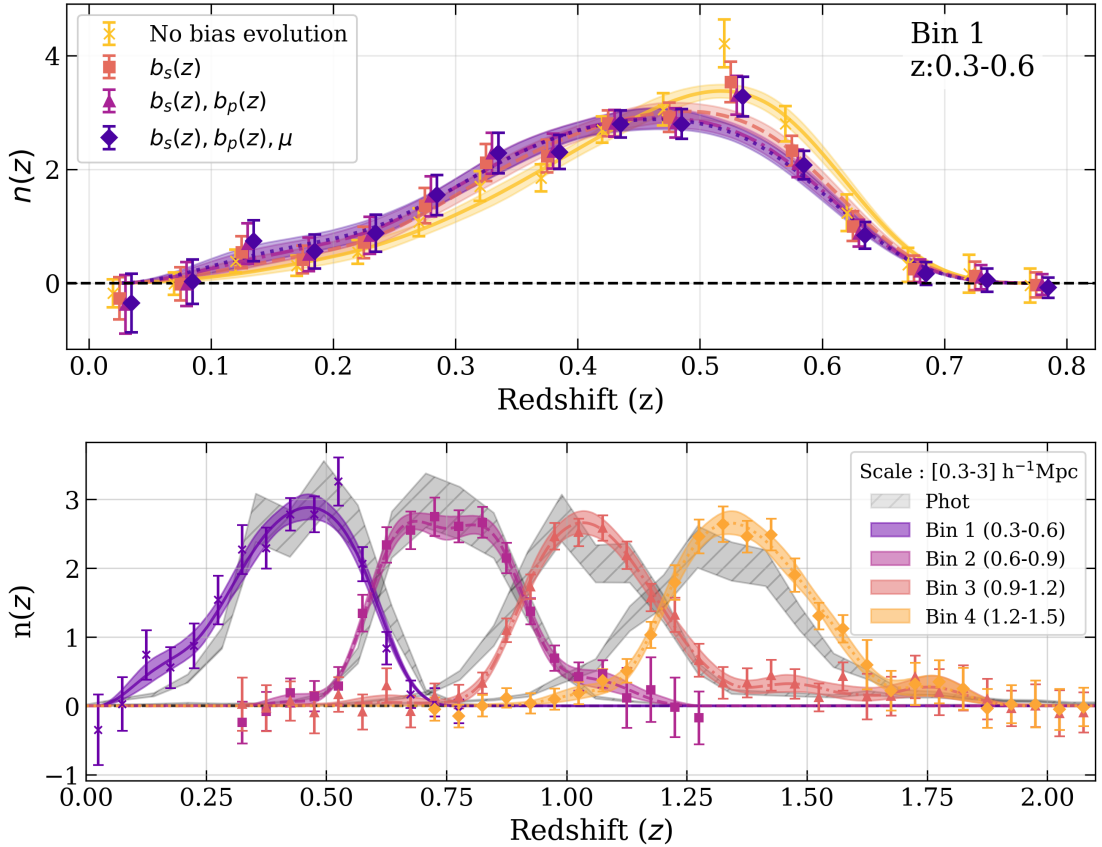


**Figure 6:** *Upper panel:* Calibrated distributions on tomographic Bin 1 ( $z \sim 0.3 - 0.6$ ), showing the impact of the different corrections on the shape of the distribution. For each color, we include an additional correction. No bias evolution corresponds to only using cross-correlations with dark matter evolution.  $b(z)$  corrections account for spectroscopic galaxy bias with auto-correlations ( $b_s(z)$ ), and photometric galaxy bias ( $b_p(z)$ ), as described in section 3.4. Finally, the last correction are the magnification corrections  $\mu$ , described in section 3.5. Measurements are offset for readability. We observe similar shifts with these corrections for all bins, as displayed in Table 5 and Figure 7. *Lower panel:* Model distributions on each of the 4 tomographic bins, with the clustering redshift measurements and the photometry calibrated distributions **PhotZ** (in hatched gray) replicated from Figure 8 of [1]. Distributions are shown with all corrections included.

as displayed in Figure 7. We explain this discrepancy with the successive corrections to correct galaxy bias with the auto-correlation measurements. With the "No bias evolution" correction, the measurement is  $n_p(z_j) \propto \bar{\omega}_{sp}(z_j)/\bar{\omega}_{mm}(z_j)$  and is more in-line with reported measurements of **WX** from the CAMIRA LRG sample. Moreover, as reported by Table 2, the BGS galaxies ( $z \sim 0 - 0.5$ ) have strong bias evolution, hence provoking significant shifts towards lower redshift expectations. This linear galaxy bias measurement is further corroborated by two-point angular measurements used in the auto-correlation correction. Note that clustering redshifts measurements of  $n(z)$  that do not take into account galaxy bias evolution are not necessarily comparable due to evolution rate differences from different calibration samples, hence partially explaining the mild difference we see between **PhotZ** &

**Table 5:** *HSC calibration results:* Measurements from the clustering redshift analysis [1]. The **PhotZ** calibration measurements correspond to the hatched gray background curves from photometry calibration shown in Figure 6 and in Figure 8 of [1]. **WX** adds in calibration from the clustering redshifts measurements with the **CAMIRA** LRG sample. The Bayesian surprise term is the Kullback-Leibler divergence, characterizing the information gained from the addition of cross-correlations over the **PhotZ** calibration. Values in brackets are the standard deviation for the considered measurement. For the following table sections, measurements displayed correspond to shifts with respect to the "Y3 Total" measurement. A negative shift denotes a shift of the new measurements towards higher redshifts. *Cosmic Shear Results:* For Y3 power spectrum and real space cosmic shear measurements, uniform prior  $\mathcal{U}(-1,1)$  was set on the shift parameters: the measurements in the table report the mode of the posterior distribution. Y3 CSR and Y3 GC-WL respectively correspond to the photo- $z$  shift measurements performed using Cosmic Shear Ratios (CSR) [57] and the combined information from Galaxy Clustering and Weak Lensing (GC-WL) [58]. *This work:* Shifts measured for two scale cuts  $0.3 - 3 h^{-1}\text{Mpc}$  and  $1 - 5 h^{-1}\text{Mpc}$ , excluding magnification corrections (first row) and including the magnification corrections (second row) for all four tomographic bins. The sections *Cosmic Shear Results* and *This work* showcase the results as shifts with respect to the Y3 Total measurements.

Measurement	Bin 1	Bin 2	Bin 3	Bin 4
<b>HSC calibration results [1]</b>				
<b>Y3 PhotZ (DNNz)</b>	0.463 [0.005]	0.766 [0.004]	1.084 [0.004]	1.330 [0.003]
<b>Y3 DEMPz</b>	0.463	0.777	1.097	1.350
<b>Y3 PhotoZ &amp; WX</b>	0.452 [0.004]	0.766 [0.003]	1.081 [0.004]	-
<b>Y3 Bayesian Surprise</b>	3.84	0.10	0.28	-
<b>Y3 Total</b>	0.452 [0.024]	0.766 [0.022]	1.081 [0.031]	1.330 [0.034]
<b>Cosmic shear results</b>				
<b>Y3 Power Spectrum [9]</b>	-	-	$-0.075^{+0.056}_{-0.059}$	$-0.157^{+0.094}_{-0.111}$
<b>Y3 Real Space [8]</b>	-	-	$-0.115^{+0.052}_{-0.058}$	$-0.192^{+0.088}_{-0.088}$
<b>Y3 CSR [57]</b>	-	$+0.002^{+0.021}_{-0.022}$	$-0.002^{+0.085}_{-0.217}$	$-0.292^{+0.229}_{-0.324}$
<b>Y3 GC-WL [58]</b>	-	-	$-0.112^{+0.046}_{-0.049}$	$-0.185^{+0.071}_{-0.081}$
<b>This work, [0.3, 3] <math>h^{-1}\text{Mpc}</math></b>				
<b>B-spline   <math>b_s(z), b_p(z)</math></b>	$+0.025^{+0.008}_{-0.008}$	$-0.009^{+0.008}_{-0.008}$	$-0.041^{+0.019}_{-0.018}$	$-0.048^{+0.012}_{-0.011}$
<b>B-spline   <math>b_s(z), b_p(z), \mu</math></b>	$+0.029^{+0.008}_{-0.008}$	$-0.003^{+0.009}_{-0.009}$	$-0.039^{+0.020}_{-0.021}$	$-0.048^{+0.012}_{-0.012}$
<b>This work, [1, 5] <math>h^{-1}\text{Mpc}</math></b>				
<b>B-spline   <math>b_s(z), b_p(z)</math></b>	$+0.026^{+0.013}_{-0.013}$	$-0.022^{+0.014}_{-0.013}$	$-0.036^{+0.028}_{-0.025}$	$-0.056^{+0.016}_{-0.015}$
<b>B-spline   <math>b_s(z), b_p(z), \mu</math></b>	$+0.028^{+0.013}_{-0.014}$	$-0.019^{+0.015}_{-0.014}$	$-0.033^{+0.030}_{-0.026}$	$-0.055^{+0.017}_{-0.016}$

**WX** and the measurement with no bias evolution made in this work.

In Bin 2, we observe full consistency with the HSC Y3 results for both scale cuts. This result is consistent with the Cosmic Shear Ratio photo- $z$  [57] calibration. Bin 2 has the highest relative magnification correction: still, magnification has a minor effect with respect to the other corrections made to the  $n(z)$  measurement. In Bin 2, we decide to not use

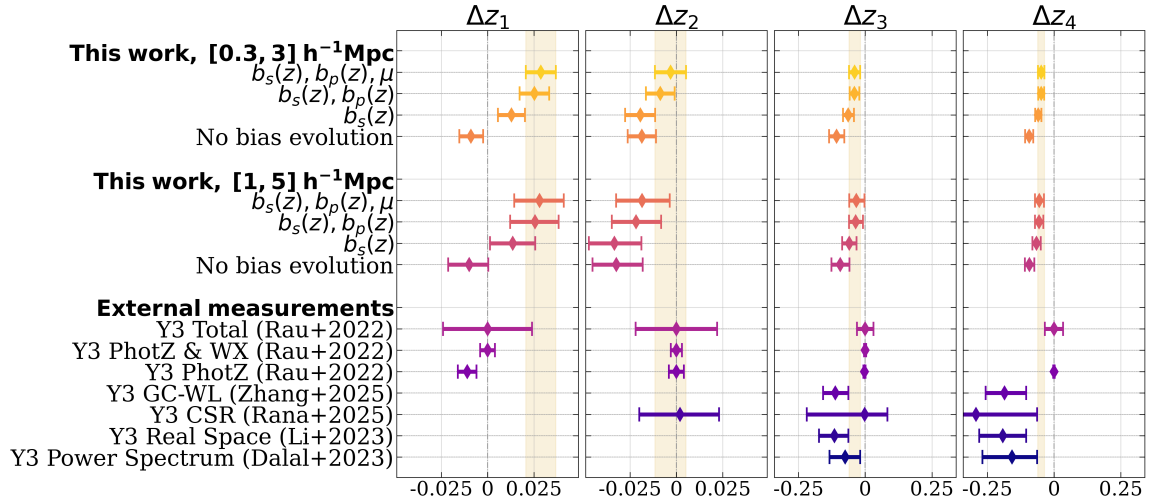


**Figure 7:** Shift values for each of the 4 tomographic bins in the catalog from posterior draws compared to Y3 Total, Y3 **PhotZ**, Y3 **PhotZ & WX** described in [1] and replicated in Table 5. Note that the **PhotZ** errors do not include systematics, and that **WX** has incomplete redshift coverage, or is completely absent, for Bin 3 and Bin 4, respectively. The results are compared to Cosmic Shear Ratio (CSR) [57] photo- $z$  shift calibration, combined galaxy clustering and weak lensing (GC-WL) [58] shift measurements, angular power spectrum cosmic shear [9], and two-point correlation cosmic shear [8] posterior modes. We display the effect of the successive corrections to  $n(z)$ . No bias evolution corresponds to only using the cross-correlations with dark matter evolution over the bin.  $b_s(z)$  and  $b_p(z)$  respectively correspond to the corrections of the bias evolution for the spectroscopic sample and the photometric sample, discussed in sections 3.3 and 3.4. When correcting only for  $b_s(z)$ , we take into account dark matter evolution. Finally,  $\mu$  is the magnification correction detailed in section 3.5. We showcase the impact of choosing a different, more conservative scale cut such as  $1 - 5 h^{-1} \text{Mpc}$ . The shaded gold area corresponds to our fiducial result with all calibrations included over scales  $0.3 - 3 h^{-1} \text{Mpc}$ , projected to compare with other measurements.

ELGs from DR1 as they are subject to significant fiber collisions: about  $\sim 35\%$  of ELGs were observed in DR1, resulting in approximately  $\sim 50\%$  missing small-scale pairs [91]. This effect is much less significant at larger scales  $1 - 5 h^{-1} \text{Mpc}$  as we leave the regime of small-scale fiber assignment issues, especially for the higher redshift range. The consistency showcased between our measurements at different scales furthermore supports that fiber assignment systematics do not introduce bias in the measurements, as detailed in section 4. We notice Bin 2 presents minor shifts with respect to the smaller scale measurements, however this seems entirely driven by a single redshift bin and subsequently unrelated to fiber assignment issues. In contrast, the large scale incompleteness is corrected by the completeness weights included in the measurements. With subsequent data releases for DESI, the ELG completeness and fiber assignment issues are expected to significantly improve. In that regard, further improving these measurements is left for future work.

Bin 3 and Bin 4 leverage the DESI DR2 dataset for the calibrated  $n(z)$ . Due to their high galaxy bias, the measurements for the QSO sample offer very good insights in calibrating high-redshift ranges, despite the low number densities reported in Figure 2. We measure a shift towards higher redshifts: however, the shift is less strong than the shifts predicted by

GC-WL and cosmic shear analyses. CSR analysis for Bin 3 shows better consistency with the shifts inferred in the present work, though the larger error bars allow the measurement to remain consistent with the remaining calibrations. Moreover, in Bin 3, the **PhotZ** calibration predicted significant tail-like effects on the high redshift range  $z \sim 1.3 - 1.8$ . While Bin 3 has partial clustering redshifts measurements to calibrate the distributions in [1], the tail-like effect is not probed by cross-correlations due to the limited redshift range of the CAMIRA LRG sample ( $z \lesssim 1.2$ ). The tail contribution is measured in this analysis and we find it has stronger amplitude than initially expected by the **PhotZ** distribution, as shown in Figure 6. This can be used to explain our noticeable shift in the tomographic mean with respect to the calibration provided in the first analysis, where clustering measurements spanned up to  $z \sim 1.2$  and therefore did not have clustering insights for the tail effects. This result is more in-line with the expected possible shift in  $\Delta z_3$  reported by the cosmic shear analyses [8, 9], though still lower than reported by these analyses. In the lower panel of Figure 6, we show the  $n(z)$  distributions for the four tomographic bins on the same figure. We underlay the figure with the hatched distributions from **PhotZ** calibration for each of the bins. When it comes to cosmology dependence of these results, they are two-fold: cosmology impacts the scale cuts we define for this analysis, and cosmology intervenes in the dark matter auto-correlation  $\bar{\omega}_{mm}$  function. In any correction that does not include both  $b_s(z)$  and  $b_p(z)$ , we compensate our measurements with  $\bar{\omega}_{mm}(z)$ . However, if one corrects for both  $b_s(z)$  and  $b_p(z)$  with the measured auto-correlations (for example, any measurement showcased in Table 5), then  $\bar{\omega}_{mm}$  is encompassed in the auto-correlation vectors, and therefore we do not introduce cosmology dependence from the computation, except from chosen scale cuts. As reported by [1], for fairly extreme cosmologies at the  $2\sigma$  contour of Stage III surveys, one can see up to  $\sim 10\%$  effects in the redshift scaling of  $\bar{\omega}_{mm}$ . In this work, in the context of fiducial results, this dependence only affects the magnification corrections presented in section 3.5 as they rely on the theoretical dark matter auto-correlation: this scaling effect is not considered in this work with respect to the other assumptions relevant to the magnification correction.

## 7 Conclusion

In this work, we provide a full calibration of the four HSC tomographic bins, including constraints on the two higher redshift tomographic bins. With the arrival of Stage-IV weak lensing surveys such as LSST, Euclid and the Roman Space Telescope, and further spectroscopic data programs available such as the next data releases of DESI and the data acquisition of the Prime Focus Spectrograph (PFS) [99] program, systematic mitigation will become significantly more important. Therefore, this work explored reducing some of the common systematics in clustering redshifts, such as galaxy bias and magnification effects. The fiducial scale cut choice of this analysis is  $0.3 - 3 \text{ h}^{-1} \text{ Mpc}$ . Consistency between the two presented scale cuts ( $0.3 - 3 \text{ h}^{-1} \text{ Mpc}$  and  $1 - 5 \text{ h}^{-1} \text{ Mpc}$ ) alleviates concerns that bias modeling complexities have substantial impacts on the showcased results in section 6.

Our calibration of the tomographic distributions suggests smaller shifts than expected by the cosmic shear analyses from HSC Year 3 and the shear calibration ratios analysis in Bin 3 and Bin 4. This analysis also hints at biases present in Bin 1 and a mild bias present in Bin 2, both towards lower redshifts. In companion paper [100], we present the cosmological parameter inference on cosmic shear in Fourier space with the calibrated redshift distributions from this analysis.

The code used for this work and all the data to replicate the figures of this paper is made publicly available at [github.com/jeanchdjdev/desi-y3-hsc](https://github.com/jeanchdjdev/desi-y3-hsc).

## Acknowledgments

JCdJ acknowledges support from Fondation CentraleSupélec and Fondation Ailes de France. SGG acknowledges that this work was performed in part at the Aspen Center for Physics, which is supported by National Science Foundation grant PHY-2210452 and a grant from the Alfred P Sloan Foundation (G-2024-22395). US is supported by NSF CDSE grant number AST-2408026 and NASA TCAN grant number 80NSSC24K0101. TZ is supported by Schmidt Sciences.

This research used data obtained with the Dark Energy Spectroscopic Instrument (DESI). DESI construction and operations is managed by the Lawrence Berkeley National Laboratory. This material is based upon work supported by the U.S. Department of Energy, Office of Science, Office of High-Energy Physics, under Contract No. DE-AC02-05CH11231, and by the National Energy Research Scientific Computing Center, a DOE Office of Science User Facility under the same contract. Additional support for DESI was provided by the U.S. National Science Foundation (NSF), Division of Astronomical Sciences under Contract No. AST-0950945 to the NSF's National Optical-Infrared Astronomy Research Laboratory; the Science and Technology Facilities Council of the United Kingdom; the Gordon and Betty Moore Foundation; the Heising-Simons Foundation; the French Alternative Energies and Atomic Energy Commission (CEA); the National Council of Humanities, Science and Technology of Mexico (CONAHCYT); the Ministry of Science and Innovation of Spain (MICINN), and by the DESI Member Institutions: [www.desi.lbl.gov/collaborating-institutions](http://www.desi.lbl.gov/collaborating-institutions). The DESI collaboration is honored to be permitted to conduct scientific research on I'oligam Du'ag (Kitt Peak), a mountain with particular significance to the Tohono O'odham Nation. Any opinions, findings, and conclusions or recommendations expressed in this material are those of the author(s) and do not necessarily reflect the views of the U.S. National Science Foundation, the U.S. Department of Energy, or any of the listed funding agencies.

The Hyper Suprime-Cam (HSC) collaboration includes the astronomical communities of Japan and Taiwan, and Princeton University. The HSC instrumentation and software were developed by the National Astronomical Observatory of Japan (NAOJ), the Kavli Institute for the Physics and Mathematics of the Universe (Kavli IPMU), the University of Tokyo, the High Energy Accelerator Research Organization (KEK), the Academia Sinica Institute for Astronomy and Astrophysics in Taiwan (ASIAA), and Princeton University. Funding was contributed by the FIRST program from the Japanese Cabinet Office, the Ministry of Education, Culture, Sports, Science and Technology (MEXT), the Japan Society for the Promotion of Science (JSPS), Japan Science and Technology Agency (JST), the Toray Science Foundation, NAOJ, Kavli IPMU, KEK, ASIAA, and Princeton University. This paper makes use of software developed for Vera C. Rubin Observatory. We thank the Rubin Observatory for making their code available as free software at <http://pipelines.lsst.io/>. This paper is based on data collected at the Subaru Telescope and retrieved from the HSC data archive system, which is operated by the Subaru Telescope and Astronomy Data Center (ADC) at NAOJ. Data analysis was in part carried out with the cooperation of Center for Computational Astrophysics (CfCA), NAOJ. We are honored and grateful for the opportunity of observing the universe from Maunakea, which has the cultural, historical and natural significance in Hawai'i.

This analysis used the following software packages: `astropy` [68, 101, 102], `CCL` [76], `Corrfunc` [85, 86] (with `cosmodesi/pycorr`), `mocpy` [87], `numpy` [103], `SciPy` [104], `matplotlib` [105], `pyMC` [98], `scikit-learn` [97], `fitsio`.

## References

- [1] M.M. Rau, R. Dalal, T. Zhang, X. Li, A.J. Nishizawa, S. More et al., *Weak lensing tomographic redshift distribution inference for the hyper supprime-cam subaru strategic program three-year shape catalogue*, *Monthly Notices of the Royal Astronomical Society* **524** (2023) 5109–5131.
- [2] H. Aihara, Y. AlSayyad, M. Ando, R. Armstrong, J. Bosch, E. Egami et al., *Third data release of the hyper supprime-cam subaru strategic program*, *Publications of the Astronomical Society of Japan* **74** (2022) 247–272.
- [3] T.M.C. Abbott, F.B. Abdalla, S. Allam, A. Amara, J. Annis, J. Asorey et al., *The Dark Energy Survey: Data Release 1*, *ApJS* **239** (2018) 18 [1801.03181].
- [4] A.H. Wright et al., *The fifth data release of the Kilo Degree Survey: Multi-epoch optical/NIR imaging covering wide and legacy-calibration fields*, *Astron. Astrophys.* **686** (2024) A170 [2503.19439].
- [5] O. Doré, C. Hirata, Y. Wang, D. Weinberg, T. Eifler, R.J. Foley et al., *Wfirst: The essential cosmology space observatory for the coming decade*, 1904.01174.
- [6] Y. Mellier, Abdurro’uf, J.A. Acevedo Barroso, A. Achúcarro, J. Adamek, R. Adam et al., *Euclid: I. overview of the euclid mission*, *A&A* **697** (2025) A1.
- [7] Ž. Ivezić, S.M. Kahn, J.A. Tyson, B. Abel, E. Acosta, R. Allsman et al., *LSST: From Science Drivers to Reference Design and Anticipated Data Products*, *ApJ* **873** (2019) 111 [0805.2366].
- [8] X. Li, T. Zhang, S. Sugiyama, R. Dalal, R. Terasawa, M.M. Rau et al., *Hyper supprime-cam year 3 results: Cosmology from cosmic shear two-point correlation functions*, 2304.00702.
- [9] R. Dalal, X. Li, A. Nicola, J. Zuntz, M.A. Strauss, S. Sugiyama et al., *Hyper supprime-cam year 3 results: Cosmology from cosmic shear power spectra*, *Physical Review D* **108** (2023) .
- [10] A. Amon, D. Gruen, M. Troxel, N. MacCrann, S. Dodelson, A. Choi et al., *Dark energy survey year 3 results: Cosmology from cosmic shear and robustness to data calibration*, *Physical Review D* **105** (2022) .
- [11] L. Secco, S. Samuroff, E. Krause, B. Jain, J. Blazek, M. Raveri et al., *Dark energy survey year 3 results: Cosmology from cosmic shear and robustness to modeling uncertainty*, *Physical Review D* **105** (2022) .
- [12] M. Asgari, C.-A. Lin, B. Joachimi, B. Giblin, C. Heymans, H. Hildebrandt et al., *Kids-1000 cosmology: Cosmic shear constraints and comparison between two point statistics*, *A&A* **645** (2021) A104.
- [13] A.H. Wright, B. Stözlner, M. Asgari, M. Bilicki, B. Giblin, C. Heymans et al., *Kids-legacy: Cosmological constraints from cosmic shear with the complete kilo-degree survey*, 2503.19441.
- [14] O. Ilbert, S. Arnouts, H.J. McCracken, M. Bolzonella, E. Bertin, O. Le Fèvre et al., *Accurate photometric redshifts for the CFHT legacy survey calibrated using the VIMOS VLT deep survey*, *A&A* **457** (2006) 841.
- [15] S. Arnouts, S. Cristiani, L. Moscardini, S. Matarrese, F. Lucchin, A. Fontana et al., *Measuring and modelling the redshift evolution of clustering: the Hubble Deep Field North*, *MNRAS* **310** (1999) 540 [astro-ph/9902290].
- [16] G.B. Brammer, P.G. van Dokkum and P. Coppi, *Eazy: A fast, public photometric redshift code*, *The Astrophysical Journal* **686** (2008) 1503–1513.

- [17] M. Tanaka, *Photometric redshift with bayesian priors on physical properties of galaxies*, *The Astrophysical Journal* **801** (2015) 20.
- [18] M. Carrasco Kind and R.J. Brunner, *Somz: photometric redshift pdfs with self-organizing maps and random atlas*, *Monthly Notices of the Royal Astronomical Society* **438** (2014) 3409–3421.
- [19] B.C. Hsieh and H.K.C. Yee, *Estimating luminosities and stellar masses of galaxies photometrically without determining redshifts*, *The Astrophysical Journal* **792** (2014) 102.
- [20] A. Collister and O. Lahav, *Annz: Estimating photometric redshifts using artificial neural networks*, *Publications of the Astronomical Society of the Pacific* **116** (2004) 345–351.
- [21] A.H. Wright, H. Hildebrandt, J.L. van den Busch, M. Bilicki, C. Heymans, B. Joachimi et al., *Kids-legacy: Redshift distributions and their calibration*, **2503.19440**.
- [22] A.H. Wright, H. Hildebrandt, J.L. van den Busch and C. Heymans, *Photometric redshift calibration with self-organising maps*, *A&A* **637** (2020) A100.
- [23] A. Campos, B. Yin, S. Dodelson, A. Amon, A. Alarcon, C. Sánchez et al., *Enhancing weak lensing redshift distribution characterization by optimizing the dark energy survey self-organizing map photo-z method*, **2408.00922**.
- [24] H. Hildebrandt, J.L. van den Busch, A.H. Wright, C. Blake, B. Joachimi, K. Kuijken et al., *Kids-1000 catalogue: Redshift distributions and their calibration*, *A&A* **647**.
- [25] D.C. Masters, D.K. Stern, J.G. Cohen, P.L. Capak, J.D. Rhodes, F.J. Castander et al., *The complete calibration of the color–redshift relation (c3r2) survey: Survey overview and data release 1*, *The Astrophysical Journal* **841** (2017) 111.
- [26] R. Buchs, C. Davis, D. Gruen, J. DeRose, A. Alarcon, G.M. Bernstein et al., *Phenotypic redshifts with self-organizing maps: A novel method to characterize redshift distributions of source galaxies for weak lensing*, *Monthly Notices of the Royal Astronomical Society* **489** (2019) 820–841.
- [27] M. Lima, C.E. Cunha, H. Oyaizu, J. Frieman, H. Lin and E.S. Sheldon, *Estimating the redshift distribution of photometric galaxy samples*, *MNRAS* **390** (2008) 118 [0801.3822].
- [28] J.A. Newman, *Calibrating redshift distributions beyond spectroscopic limits with cross-correlations*, *The Astrophysical Journal* **684** (2008) 88.
- [29] B. Ménard, R. Scranton, S. Schmidt, C. Morrison, D. Jeong, T. Budavari et al., *Clustering-based redshift estimation: method and application to data*, **1303.4722**.
- [30] M. Gatti, P. Vielzeuf, C. Davis, R. Cawthon, M.M. Rau, J. DeRose et al., *Dark energy survey year 1 results: cross-correlation redshifts – methods and systematics characterization*, *Monthly Notices of the Royal Astronomical Society* **477** (2018) 1664 [<https://academic.oup.com/mnras/article-pdf/477/2/1664/25009657/sty466.pdf>].
- [31] M. Gatti, P. Vielzeuf, C. Davis, R. Cawthon, M.M. Rau, J. DeRose et al., *Dark energy survey year 1 results: cross-correlation redshifts – methods and systematics characterization*, *Monthly Notices of the Royal Astronomical Society* **477** (2018) 1664–1682.
- [32] M. Gatti, G. Giannini, G.M. Bernstein, A. Alarcon, J. Myles, A. Amon et al., *Dark energy survey year 3 results: clustering redshifts – calibration of the weak lensing source redshift distributions with redmagic and boss/eboss*, *Monthly Notices of the Royal Astronomical Society* **510** (2021) 1223–1247.
- [33] R. Cawthon, J. Elvin-Poole, A. Porredon, M. Crocce, G. Giannini, M. Gatti et al., *Dark energy survey year 3 results: calibration of lens sample redshift distributions using clustering redshifts with boss/eboss*, *Monthly Notices of the Royal Astronomical Society* **513** (2022) 5517 [<https://academic.oup.com/mnras/article-pdf/513/4/5517/43865105/stac1160.pdf>].

- [34] C. Davis, M. Gatti, P. Vielzeuf, R. Cawthon, E. Rozo, A. Alarcon et al., *Dark energy survey year 1 results: Cross-correlation redshifts in the des – calibration of the weak lensing source redshift distributions*, [1710.02517](#).
- [35] W. d’Assignies Doumerg, M. Manera, C. Padilla, O. Ilbert, H. Hildebrandt, L. Reynolds et al., *Euclid: Photometric redshift calibration with the clustering redshifts technique*, [2505.10416](#).
- [36] J.L. van den Busch, H. Hildebrandt, A.H. Wright, C.B. Morrison, C. Blake, B. Joachimi et al., *Testing kids cross-correlation redshifts with simulations*, [A&A 642 \(2020\) A200](#).
- [37] C.B. Morrison, H. Hildebrandt, S.J. Schmidt, I.K. Baldry, M. Bilicki, A. Choi et al., *the-wizz: clustering redshift estimation for everyone*, [Monthly Notices of the Royal Astronomical Society 467 \(2017\) 3576–3589](#).
- [38] S.J. Schmidt, B. Ménard, R. Scranton, C. Morrison and C.K. McBride, *Recovering redshift distributions with cross-correlations: pushing the boundaries*, [Monthly Notices of the Royal Astronomical Society 431 \(2013\) 3307–3318](#).
- [39] M. McQuinn and M. White, *On using angular cross-correlations to determine source redshift distributions*, [Monthly Notices of the Royal Astronomical Society 433 \(2013\) 2857–2883](#).
- [40] X. Li, H. Miyatake, W. Luo, S. More, M. Oguri, T. Hamana et al., *The three-year shear catalog of the subaru hyper supprime-cam ssp survey*, [Publications of the Astronomical Society of Japan 74 \(2022\) 421–459](#).
- [41] DESI Collaboration, M. Abdul-Karim, A.G. Adame, D. Aguado, J. Aguilar, S. Ahlen et al., *Data Release 1 of the Dark Energy Spectroscopic Instrument*, [arXiv e-prints \(2025\) arXiv:2503.14745 \[2503.14745\]](#).
- [42] DESI Collaboration, “Data Release 2 of the Dark Energy Spectroscopic Instrument.”.
- [43] DESI Collaboration, A. Aghamousa, J. Aguilar, S. Ahlen, S. Alam, L.E. Allen et al., *The DESI Experiment Part II: Instrument Design*, [arXiv e-prints \(2016\) arXiv:1611.00037 \[1611.00037\]](#).
- [44] DESI Collaboration, B. Abareshi, J. Aguilar, S. Ahlen, S. Alam, D.M. Alexander et al., *Overview of the Instrumentation for the Dark Energy Spectroscopic Instrument*, [AJ 164 \(2022\) 207 \[2205.10939\]](#).
- [45] T.N. Miller, P. Doel, G. Gutierrez, R. Besuner, D. Brooks, G. Gallo et al., *The Optical Corrector for the Dark Energy Spectroscopic Instrument*, [AJ 168 \(2024\) 95 \[2306.06310\]](#).
- [46] C. Poppett, L. Tyas, J. Aguilar, C. Bebek, D. Bramall, T. Claybaugh et al., *Overview of the Fiber System for the Dark Energy Spectroscopic Instrument*, [AJ 168 \(2024\) 245](#).
- [47] J. Guy, S. Bailey, A. Kremin, S. Alam, D.M. Alexander, C. Allende Prieto et al., *The Spectroscopic Data Processing Pipeline for the Dark Energy Spectroscopic Instrument*, [AJ 165 \(2023\) 144 \[2209.14482\]](#).
- [48] E.F. Schlafly, D. Kirkby, D.J. Schlegel, A.D. Myers, A. Raichoor, K. Dawson et al., *Survey Operations for the Dark Energy Spectroscopic Instrument*, [AJ 166 \(2023\) 259 \[2306.06309\]](#).
- [49] C. Hahn, M.J. Wilson, O. Ruiz-Macias, S. Cole, D.H. Weinberg, J. Moustakas et al., *The desi bright galaxy survey: Final target selection, design, and validation*, [AJ 165 \(2023\) 253](#).
- [50] R. Zhou, B. Dey, J.A. Newman, D.J. Eisenstein, K. Dawson, S. Bailey et al., *Target selection and validation of desi luminous red galaxies*, [AJ 165 \(2023\) 58](#).
- [51] A. Raichoor, J. Moustakas, J.A. Newman, T. Karim, S. Ahlen, S. Alam et al., *Target selection and validation of desi emission line galaxies*, [AJ 165 \(2023\) 126](#).
- [52] E. Chaussidon, C. Yèche, N. Palanque-Delabrouille, D.M. Alexander, J. Yang, S. Ahlen et al., *Target selection and validation of desi quasars*, [The Astrophysical Journal 944 \(2023\) 107](#).

- [53] DESI Collaboration, M. Abdul-Karim, J. Aguilar, S. Ahlen, S. Alam, L. Allen et al., *DESI DR2 Results II: Measurements of Baryon Acoustic Oscillations and Cosmological Constraints*, *arXiv e-prints* (2025) arXiv:2503.14738 [2503.14738].
- [54] DESI Collaboration, A.G. Adame, J. Aguilar, S. Ahlen, S. Alam, D.M. Alexander et al., *DESI 2024 VII: Cosmological Constraints from the Full-Shape Modeling of Clustering Measurements*, *arXiv e-prints* (2024) arXiv:2411.12022 [2411.12022].
- [55] H. Aihara, N. Arimoto, R. Armstrong, S. Arnouts, N.A. Bahcall, S. Bickerton et al., *The hyper supprime-cam ssp survey: Overview and survey design*, *Publications of the Astronomical Society of Japan* **70** (2017) .
- [56] T. Zhang, M.M. Rau, R. Mandelbaum, X. Li and B. Moews, *Photometric redshift uncertainties in weak gravitational lensing shear analysis: models and marginalization*, *Monthly Notices of the Royal Astronomical Society* **518** (2022) 709–723.
- [57] D. Rana, S. More, H. Miyatake, S. Sugiyama, T. Zhang and M. Shirasaki, *Hyper supprime-cam y3 results: photo-z bias calibration with lensing shear ratios and cosmological constraints from cosmic shea*, *Physical Review D* (2025) [2508.21681].
- [58] T. Zhang, X. Li, S. Sugiyama, R. Mandelbaum, S. More, R. Dalal et al., *Cosmology and Source Redshift Constraints from Galaxy Clustering and Tomographic Weak Lensing with HSC Y3 and SDSS using the Point-Mass Correction Model*, *arXiv e-prints* (2025) arXiv:2507.01386 [2507.01386].
- [59] A.J. Ross, J. Aguilar, S. Ahlen, S. Alam, A. Anand, S. Bailey et al., *The construction of large-scale structure catalogs for the Dark Energy Spectroscopic Instrument*, *J. Cosmology Astropart. Phys.* **2025** (2025) 125 [2405.16593].
- [60] A. Adame, J. Aguilar, S. Ahlen, S. Alam, D. Alexander, M. Alvarez et al., *Desi 2024 ii: sample definitions, characteristics, and two-point clustering statistics*, *Journal of Cosmology and Astroparticle Physics* **2025** (2025) 017.
- [61] A.J. Nishizawa, B.-C. Hsieh, M. Tanaka and T. Takata, *Photometric redshifts for the hyper supprime-cam subaru strategic program data release 2*, **2003.01511**.
- [62] T. Zhang, X. Li, R. Dalal, R. Mandelbaum, M.A. Strauss, A. Kannawadi et al., *A general framework for removing point-spread function additive systematics in cosmological weak lensing analysis*, *Monthly Notices of the Royal Astronomical Society* **525** (2023) 2441–2471.
- [63] M. Tanaka, J. Coupon, B.-C. Hsieh, S. Mineo, A.J. Nishizawa, J. Speagle et al., *Photometric redshifts for hyper supprime-cam subaru strategic program data release 1*, *Publications of the Astronomical Society of Japan* **70** (2017) .
- [64] E. Krause, X. Fang, S. Pandey, L.F. Secco, O. Alves, H. Huang et al., *Dark Energy Survey Year 3 Results: Multi-Probe Modeling Strategy and Validation*, *arXiv e-prints* (2021) arXiv:2105.13548 [2105.13548].
- [65] T. Baldauf, R.E. Smith, U. Seljak and R. Mandelbaum, *Algorithm for the direct reconstruction of the dark matter correlation function from weak lensing and galaxy clustering*, *Phys. Rev. D* **81** (2010) 063531 [0911.4973].
- [66] D.N. Limber, *The Analysis of Counts of the Extragalactic Nebulae in Terms of a Fluctuating Density Field.*, *ApJ* **117** (1953) 134.
- [67] K. Naidoo, H. Johnston, B. Joachimi, J.L. van den Busch, H. Hildebrandt, O. Ilbert et al., *Euclid: Calibrating photometric redshifts with spectroscopic cross-correlations*, *A&A* **670** (2023) A149.
- [68] Astropy Collaboration, A.M. Price-Whelan, P.L. Lim, N. Earl, N. Starkman, L. Bradley et al., *The Astropy Project: Sustaining and Growing a Community-oriented Open-source Project and the Latest Major Release (v5.0) of the Core Package*, *ApJ* **935** (2022) 167 [2206.14220].

- [69] G. Giannini, A. Alarcon, M. Gatti, A. Porredon, M. Crocce, G.M. Bernstein et al., *Dark energy survey year 3 results: redshift calibration of the maglim lens sample from the combination of sompz and clustering and its impact on cosmology*, *Monthly Notices of the Royal Astronomical Society* **527** (2023) 2010 [<https://academic.oup.com/mnras/article-pdf/527/2/2010/53273780/stad2945.pdf>].
- [70] A. Nicola, D. Alonso, J. Sánchez, A. Slosar, H. Awan, A. Broussard et al., *Tomographic galaxy clustering with the Subaru Hyper Suprime-Cam first year public data release*, *J. Cosmology Astropart. Phys.* **2020** (2020) 044 [1912.08209].
- [71] J. Elvin-Poole, N. MacCrann, S. Everett, J. Prat, E.S. Rykoff, J. De Vicente et al., *Dark energy survey year 3 results: magnification modelling and impact on cosmological constraints from galaxy clustering and galaxy-galaxy lensing*, *Monthly Notices of the Royal Astronomical Society* **523** (2023) 3649–3670.
- [72] R. Zhou, S. Ferraro, M. White, J. DeRose, N. Sailer, J. Aguilar et al., *Desi luminous red galaxy samples for cross-correlations*, *Journal of Cosmology and Astroparticle Physics* **2023** (2023) 097.
- [73] M. von Wietersheim Kramsta, B. Joachimi, J.L. van den Busch, C. Heymans, H. Hildebrandt, M. Asgari et al., *Magnification bias in galaxy surveys with complex sample selection functions*, *Monthly Notices of the Royal Astronomical Society* **504** (2021) 1452 [<https://academic.oup.com/mnras/article-pdf/504/1/1452/39571307/stab1000.pdf>].
- [74] A. Choi, C. Heymans, C. Blake, H. Hildebrandt, C.A.J. Duncan, T. Erben et al., *Cfhtlens and rclsens: testing photometric redshift distributions using angular cross-correlations with spectroscopic galaxy surveys*, *Monthly Notices of the Royal Astronomical Society* **463** (2016) 3737 [<https://academic.oup.com/mnras/article-pdf/463/4/3737/18513459/stw2241.pdf>].
- [75] S. Heydenreich, A. Leauthaud, C. Blake, Z. Sun, J.U. Lange, T. Zhang et al., *Lensing without borders: Measurements of galaxy-galaxy lensing and projected galaxy clustering in desi dr1*, **2506.21677**.
- [76] N.E. Chisari, D. Alonso, E. Krause, C.D. Leonard, P. Bull, J. Neveu et al., *Core cosmology library: Precision cosmological predictions for lsst*, *The Astrophysical Journal Supplement Series* **242** (2019) 2.
- [77] R. Takahashi, M. Sato, T. Nishimichi, A. Taruya and M. Oguri, *Revising the halofit model for the nonlinear matter power spectrum*, *The Astrophysical Journal* **761** (2012) 152.
- [78] D. Blas, J. Lesgourgues and T. Tram, *The cosmic linear anisotropy solving system (class). part ii: Approximation schemes*, *Journal of Cosmology and Astroparticle Physics* **2011** (2011) 034–034.
- [79] P. Laurent, S. Eftekharzadeh, J.-M.L. Goff, A. Myers, E. Burtin, M. White et al., *Clustering of quasars in sdss-iv eboss: study of potential systematics and bias determination*, *Journal of Cosmology and Astroparticle Physics* **2017** (2017) 017–017.
- [80] E. Chaussidon, C. Yèche, A. de Mattia, C. Payerne, P. McDonald, A.J. Ross et al., *Constraining primordial non-gaussianity with desi 2024 lrg and qso samples*, **2411.17623**.
- [81] A. Adame, J. Aguilar, S. Ahlen, S. Alam, D. Alexander, M. Alvarez et al., *Desi 2024 iii: baryon acoustic oscillations from galaxies and quasars*, *Journal of Cosmology and Astroparticle Physics* **2025** (2025) 012.
- [82] J. Bosch, R. Armstrong, S. Bickerton, H. Furusawa, H. Ikeda, M. Koike et al., *The hyper suprime-cam software pipeline*, *Publications of the Astronomical Society of Japan* **70** (2017) S5 [[https://academic.oup.com/pasj/article-pdf/70/SP1/S5/54675369/pasj\\_70\\_sp1\\_s5.pdf](https://academic.oup.com/pasj/article-pdf/70/SP1/S5/54675369/pasj_70_sp1_s5.pdf)].
- [83] N. Sailer, J. DeRose, S. Ferraro, S.-F. Chen, R. Zhou, M. White et al., *Evolution of structure*

*growth during dark energy domination: Insights from the cross-correlation of desi galaxies with cmb lensing and galaxy magnification*, [2503.24385](#).

- [84] R. de Belsunce, A. Krolewski, S. Chiarenza, E. Chaussidon, S. Ferraro, B. Hadzhiyska et al., *Cosmology from planck cmb lensing and desi dr1 quasar tomography*, [2506.22416](#).
- [85] M. Sinha and L.H. Garrison, *CORRFUNC - a suite of blazing fast correlation functions on the CPU*, [MNRAS 491 \(2020\) 3022](#).
- [86] M. Sinha and L. Garrison, *Corrfunc: Blazing fast correlation functions with avx512f simd intrinsics*, in *Software Challenges to Exascale Computing*, A. Majumdar and R. Arora, eds., (Singapore), pp. 3–20, Springer Singapore, 2019, [https://doi.org/10.1007/978-981-13-7729-7\\_1](https://doi.org/10.1007/978-981-13-7729-7_1).
- [87] P. Fernique, T. Boch, T. Donaldson, D. Durand, W. O’Mullane, M. Reinecke et al., *MOC - HEALPix Multi-Order Coverage map Version 1.0*, [1505.02937](#).
- [88] H.A. Feldman, N. Kaiser and J.A. Peacock, *Power-Spectrum Analysis of Three-dimensional Redshift Surveys*, [ApJ 426 \(1994\) 23](#) [[astro-ph/9304022](#)].
- [89] D. Bianchi and W.J. Percival, *Unbiased clustering estimation in the presence of missing observations*, [Monthly Notices of the Royal Astronomical Society 472 \(2017\) 1106](#) [<https://academic.oup.com/mnras/article-pdf/472/1/1106/19720617/stx2053.pdf>].
- [90] D. Bianchi, M.M.S. Hanif, A.C. Rosell, J. Lasker, A.J. Ross, M. Pinon et al., *Characterization of desi fiber assignment incompleteness effect on 2-point clustering and mitigation methods for dr1 analysis*, *Journal of Cosmology and Astroparticle Physics* (2025) [[2411.12025](#)].
- [91] M. Pinon, A. de Mattia, P. McDonald, E. Burtin, V. Ruhlmann-Kleider, M. White et al., *Mitigation of desi fiber assignment incompleteness effect on two-point clustering with small angular scale truncated estimators*, *Journal of Cosmology and Astroparticle Physics* **2025** (2025) 131.
- [92] F.G. Mohammad and W.J. Percival, *Creating jackknife and bootstrap estimates of the covariance matrix for the two-point correlation function*, [Monthly Notices of the Royal Astronomical Society 514 \(2022\) 1289–1301](#).
- [93] K.M. Górski, E. Hivon, A.J. Banday, B.D. Wandelt, F.K. Hansen, M. Reinecke et al., *HEALPix: A Framework for High-Resolution Discretization and Fast Analysis of Data Distributed on the Sphere*, [ApJ 622 \(2005\) 759](#) [[astro-ph/0409513](#)].
- [94] M. Davis and P.J.E. Peebles, *A survey of galaxy redshifts. V. The two-point position and velocity correlations.*, [ApJ 267 \(1983\) 465](#).
- [95] S.D. Landy and A.S. Szalay, *Bias and Variance of Angular Correlation Functions*, [ApJ 412 \(1993\) 64](#).
- [96] M.M. Rau, C.B. Morrison, S.J. Schmidt, S. Wilson, R. Mandelbaum, Y.-Y. Mao et al., *A composite likelihood approach for inference under photometric redshift uncertainty*, [Monthly Notices of the Royal Astronomical Society 509 \(2021\) 4886](#) [<https://academic.oup.com/mnras/article-pdf/509/4/4886/41715550/stab3290.pdf>].
- [97] F. Pedregosa, G. Varoquaux, A. Gramfort, V. Michel, B. Thirion, O. Grisel et al., *Scikit-learn: Machine learning in python*, *Journal of Machine Learning Research* **12** (2011) 2825.
- [98] O. Abril-Pla, V. Andreani, C. Carroll, L. Dong, C.J. Fonnesbeck, M. Kochurov et al., *PyMC: a modern, and comprehensive probabilistic programming framework in Python*, [PeerJ Comput. Sci. 9 \(2023\)](#).
- [99] N. Tamura, N. Takato, A. Shimono, Y. Moritani, K. Yabe, Y. Ishizuka et al., *Prime Focus Spectrograph (PFS) for the Subaru telescope: overview, recent progress, and future perspectives*, in *Ground-based and Airborne Instrumentation for Astronomy VI*, C.J. Evans,

- L. Simard and H. Takami, eds., vol. 9908 of *Society of Photo-Optical Instrumentation Engineers (SPIE) Conference Series*, p. 99081M, Aug., 2016, DOI [1608.01075].
- [100] J. Choppin De Janvry, B. Dai, S. Gontcho A Gontcho, U. Seljak and T. Zhang, “Cosmic Shear constraints from HSC Year 3 with complete calibration of the tomographic redshift distributions.”
- [101] Astropy Collaboration, T.P. Robitaille, E.J. Tollerud, P. Greenfield, M. Droettboom, E. Bray et al., *Astropy: A community Python package for astronomy*, *A&A* **558** (2013) A33 [1307.6212].
- [102] Astropy Collaboration, A.M. Price-Whelan, B.M. Sipőcz, H.M. Günther, P.L. Lim, S.M. Crawford et al., *The Astropy Project: Building an Open-science Project and Status of the v2.0 Core Package*, *AJ* **156** (2018) 123 [1801.02634].
- [103] C.R. Harris, K.J. Millman, S.J. van der Walt, R. Gommers, P. Virtanen, D. Cournapeau et al., *Array programming with NumPy*, *Nature* **585** (2020) 357.
- [104] P. Virtanen, R. Gommers, T.E. Oliphant, M. Haberland, T. Reddy, D. Cournapeau et al., *SciPy 1.0: Fundamental Algorithms for Scientific Computing in Python*, *Nature Methods* **17** (2020) 261.
- [105] J.D. Hunter, *Matplotlib: A 2d graphics environment*, *Computing in Science & Engineering* **9** (2007) 90.

## A Tomographic bin widths in the photometric galaxy bias approximation

In this appendix, the effects of the width and photo- $z$  spread for the galaxy bias measurement described in section 3.4 are investigated. In the aforementioned section, the choice is to use  $\Delta z = 0.1$  tomographic bins in order to recover galaxy bias. We verify here if such an approximation is valid and verify if the fairly wide profiles of the distributions presented in Figure 4 do not significantly affect the recovered bias expression, compared to a correction where one would use much narrower tomographic bins such as in [33] ( $\Delta z = 0.02$ ). In fact, using very narrow tomographic bins to probe galaxy bias leads to its own set of difficulties, as one must take into account new systematics such as border effects with adjacent bins, validity of the Limber equation, and use spectroscopic bins with minimal data. Effects of using different tomographic bin widths for this correction were explored in [35].

For this model, we assume that the underlying photometric galaxy bias  $b_p^{\text{true}}$  follows three different forms (case a,b and c):

$$b_p^{\text{true}}(z) = \begin{cases} 1 & \text{(a, constant evolution)} \\ 1/D(z) & \text{(b, passive evolution)} \\ 1 + z^2 & \text{(c, strong evolution)} \end{cases} \quad (\text{A.1})$$

where  $D(z)$  is the factor of growth of the universe. The measured distributions for tomographic bins are assumed to follow  $n_{p_k}^{\text{meas}}(z)$  distributions where  $p_k$  are the successive tomographic bins. In this context, the  $p$  subscript is used to describe a generic tomographic bin, different from the fiducial HSC tomographic bins presented in the main corpus of this work. Case 1 will assume the  $n_{p_k}$  distributions measured in section 3.4 are the  $n_{p_k}^{\text{meas}}$  distributions for the tomographic bins. Case 2 will be treated with gaussian tomographic bins  $n_{p_k}^{\text{meas}} \sim \mathcal{N}(z_k, 0.1)$  where  $z_k$  is the center redshift of the tomographic bin  $p_k$ . We choose 0.1 in order to compare with the standard deviations observed on the tomographic bins, as

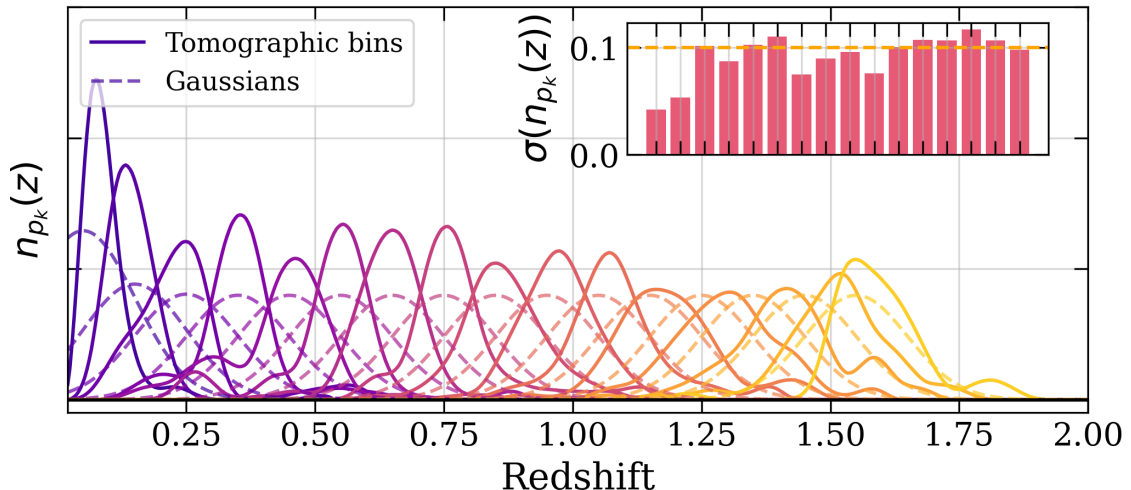


**Figure 8:** Photo- $z$   $n_{pk}^{\text{meas}}$  tomographic bins used in this model for (i) Tomographic bins derived from section 3.4 and (ii) gaussian tomographic bins  $\sim \mathcal{N}(z_k, 0.1)$  centered on the midpoint of the photometric redshift bins  $z_k$ . The inset plot of the figure showcases the standard deviation  $\sigma(n_{pk}(z))$  for the successive bins, compared to the chosen 0.1 level for the Gaussian bins scenario.

displayed in figure 8. Case 1 is shown in full lines, while case 2 is shown in dashed lines. We further add a inset figure characterizing the standard deviation of the distributions for each bin in case 1 (crimson histogram); compared to the chosen 0.1 standard deviation value assumed for the gaussian scenario (gold line). In section 3.4,  $b_p(z)\sqrt{\bar{\omega}_{mm}(z)}$  is assumed to be constant over the tomographic bin. Other works assume  $b_p(z)$  is constant over the tomographic bin: we note the quantity we consider constant in our approximation to be  $\gamma(z)$ , where  $\gamma(z) = b(z)\sqrt{\bar{\omega}_{mm}(z)}$  (method 1,  $\tilde{n}_1(z) \propto \bar{\omega}_{sp}(z)/\sqrt{\bar{\omega}_{ss}(z)}$ , used in [33] and in section 3.4) or  $\gamma(z) = b(z)$  (method 2,  $\tilde{n}_2(z) \propto \bar{\omega}_{sp}(z)/\sqrt{\bar{\omega}_{ss}(z)\bar{\omega}_{mm}(z)}$ , used in [35]). As such, the theoretical true distributions  $n_{pk}^{\text{true}}$  with respect to the measurements follow:

$$n_{pk}^{\text{true}}(z) = \frac{n_{pk}^{\text{meas}}(z) \frac{1}{\gamma(z)}}{\int_0^{+\infty} n_{pk}^{\text{meas}}(z') \frac{1}{\gamma(z')} dz'} \quad (\text{A.2})$$

Given  $b_p^{\text{true}}(z)$  usually increases with redshift,  $\sqrt{\bar{\omega}_{mm}(z)}$  and  $b_p(z)$  are competing effects. Therefore,  $\tilde{n}_1(z)$  better approximates the underlying true  $n(z)$  than  $\tilde{n}_2(z)$  for biases  $b_p^{\text{true}}(z)$  that evolve sufficiently fast. Here, sufficiently fast implies that the optimal case to recover the exact  $n(z)$  with  $\tilde{n}_1$  is obtained for  $b_p(z) \propto 1/\sqrt{\bar{\omega}_{mm}(z)}$ , while the optimal case for  $\tilde{n}_2$  is  $b_p$  constant (case a in equation A.1): one can compare the local amplitudes of  $\left| \frac{d\gamma(z)}{dz} \frac{1}{\gamma(z)} \right|$ .

The theoretical measured photometric sample cross-correlation  $\bar{\omega}_{pp}(z)$  is given by using equation 3.4 in the case of auto-correlations:

$$\bar{\omega}_{pkDk}(z_k) = \int_0^{+\infty} b_p^{\text{true}}(z)^2 n_{pk}^{\text{true}}(z)^2 \bar{\omega}_{mm}(z) dz \quad (\text{A.3})$$

Using the expression derived in section 3.4, the theoretical measured galaxy bias  $b_p^{\text{meas}}$  with

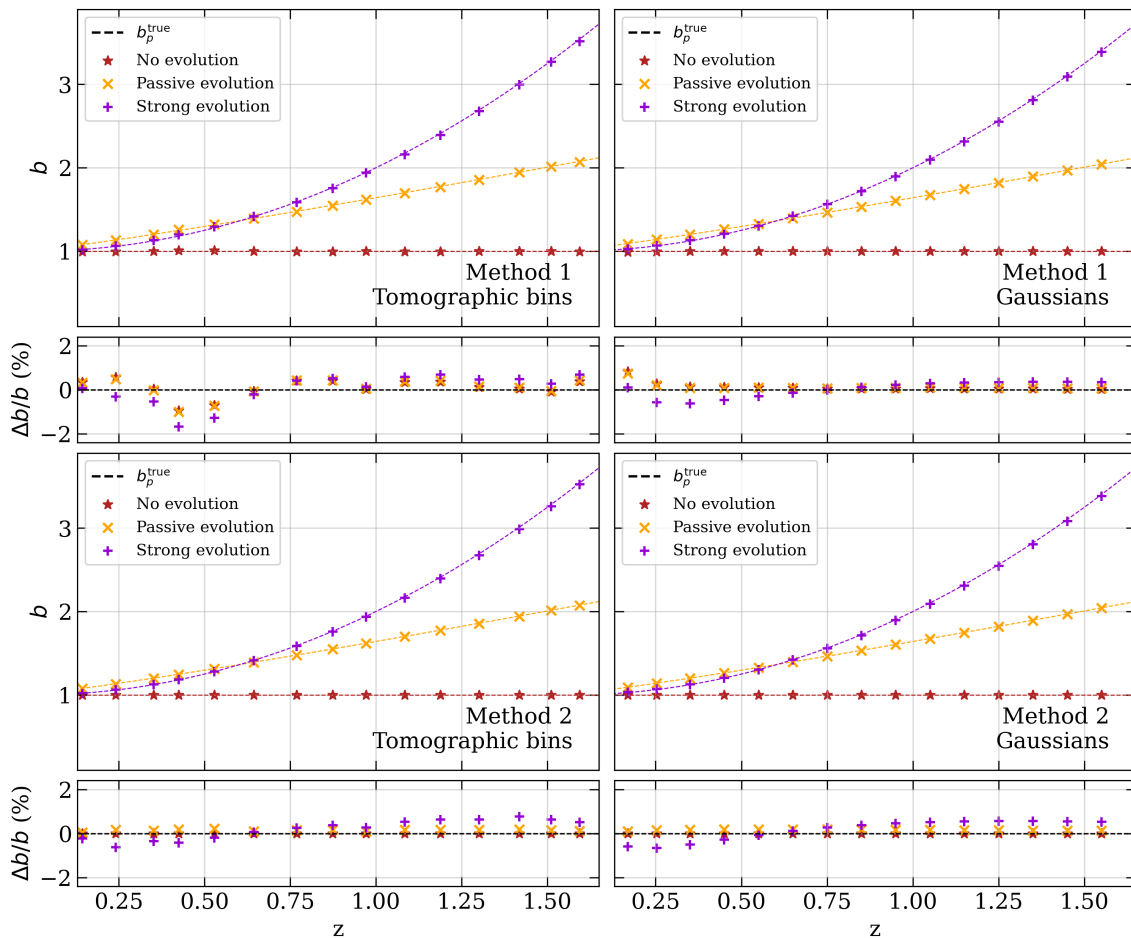


**Figure 9:** Relative error measurements on the bias for each scenario. We find that the bias deviations are contained to the % level.

the tomographic bins can be obtained:

$$b_p^{\text{meas}}(z_k) = \sqrt{\frac{\bar{\omega}_{p_k p_k}(z_k)}{\int_0^{+\infty} n_{p_k}^{\text{meas}}(z)^2 \bar{\omega}_{mm}(z) dz}} \quad (\text{A.4})$$

In figure 9, we display respectively the relative error  $\Delta b_p/b_p(z) = (b_p^{\text{meas}}(z) - b_p^{\text{true}}(z))/b_p^{\text{true}}(z)$  in percentage for each bin, as well as the reconstructed bias with tomographic bins. The relative error, just like the power law fit of section 3.4, is computed by evaluating at the expectation value of the tomographic bin. Each subplot corresponds to a different method ( $\tilde{n}_1$  or  $\tilde{n}_2$ ) or a different tomographic bin case (1 or 2) with different  $b_p^{\text{true}}(z)$  expressions. We conclude with this appendix that the tomographic bin approximation at  $\Delta z_p = 0.1$  presents no significant issues when recovering the general bias trend, since we observe local deviations from the true galaxy bias model of at most  $\sim 1.7\%$ . This result shows that the method is highly effective at recovering the global trend for galaxy bias evolution.